RESEARCH ARTICLE | JANUARY 24 2024

A numerical method to mimic an experimental wind gust generator: The immersed boundary gust generator

K. Boulbrachene ; M. Breuer

Physics of Fluids 36, 015146 (2024)
https://doi.org/10.1063/5.0187787

Physics of Fluids ARTICLE pubs.aip.org/aip/pof

A numerical method to mimic an experimental wind gust generator: The immersed boundary gust generator

Cite as: Phys. Fluids **36**, 015146 (2024); doi: 10.1063/5.0187787
Submitted: 16 November 2023 · Accepted: 27 December 2023 ·
Published Online: 24 January 2024

View Online Export Citation CrossMark

K. Boulbrachene and M. Breuer[a)]

AFFILIATIONS

Professur für Strömungsmechanik, Helmut-Schmidt-Universität Hamburg, D-22043 Hamburg, Germany

[a)]Author to whom correspondence should be addressed: breuer@hsu-hh.de

ABSTRACT

To generate horizontal wind gusts in a classical wind tunnel, Wood, Breuer, and Neumann [A novel approach for artificially generating horizontal wind gusts based on a movable plate: The paddle," J. Wind Eng. Ind. Aerodyn. 230, 105170 (2022)] developed a new wind gust generator denoted the "paddle." The working principle relies on the partial blocking of the outlet of the wind tunnel nozzle by a plate that vertically moves into the free-stream. Based on laser-Doppler anemometer measurements of the velocity at only a few locations, the basic functionality of the device was proven. The objective of the present contribution is to numerically mimic the gust generator and the flow field induced by the paddle in the test section. Contrary to the single-point measurements, the three-dimensional time-resolved simulation delivers the entire flow field and thus allows to investigate all details of the generated gust. To describe the paddle motion, the immersed boundary method with a continuous and direct forcing approach is implemented into a finite-volume flow solver for large-eddy simulations. A uniform and a non-uniform distribution of the Lagrangian markers are investigated where the latter ensures that an excessive increase in the computational resources required can be avoided. The predictions allow to characterize the resulting flow features induced by the paddle in great detail. Furthermore, a comparison of the numerical and experimental results is carried out based on the time histories of the streamwise and vertical velocity components at certain positions showing a close agreement. Finally, the forces acting on the fluid by the moving paddle are evaluated.

I. INTRODUCTION

Wind gusts are a meteorological phenomenon that is also of high interest for engineers due to their devastating consequences on structures. Especially constructions made of lightweight thin membranes such as large umbrellas, tents, or stadium roofs are vulnerable to wind events. In order to better understand the effect of strong wind gusts on such constructions, investigations on this fluid-structure interaction (FSI) scenario are necessary. Measurements at real scales can only be carried out if the building has already been constructed. Furthermore, they are extremely challenging and costly. Thus, investigations at a smaller scale are an alternative, but require to artificially generate the wind gust in the wind tunnel.

Recently, Wood, Breuer, and Neumann[1] carried out a literature review on the topic of experimental devices devised for the generation of artificial gusts. They distinguished the different methods into two classes: methods for the generation of low and high amplitude gusts. The latter class also includes the working principle of substantially blocking the wind tunnel inflow section. For example, Neunaber and Braud[2] developed a rotating bar called the *chopper* cutting through a wind tunnel inlet to model extreme gust events for wind turbines. The flow velocity depicts a spike followed by an inverse gust due to the blockage of the inlet. Thus, rapid and strong velocity fluctuations with high turbulence intensities are generated.

In order to better control the shape and the intensity of the provoked wind gust, to reach a high reproducibility and to allow the superposition of the wind gust to the free-stream flow, Wood, Breuer, and Neumann[1] developed an artificial wind gust generator (WGG) denoted the "*paddle.*" In Sec. II, the main features of this new device are explained. By partially blocking the outlet of the wind tunnel nozzle by the paddle, the flow is strongly accelerated leading to a horizontal gust. Based on laser-Doppler anemometer (LDA) measurements, the instantaneous and phase-averaged streamwise and wall-normal velocities were determined at 11 specific points in the flow field. That allowed to get a first impression of the flow field during the gust generation. However, a full two-dimensional (e.g., geometric symmetry plane) or even a full three-dimensional (e.g., entire test section) representation of the gust event could not be achieved. This gave rise to the idea that this obvious gap can be closed through appropriate numerical simulations leading to the current study.

Since the experimental setup includes the moving paddle, which blocks a part of the outlet of the nozzle for a short time interval, this specific feature has to be taken into account. One way to model this is by using a body-conforming mesh and to directly enforce the boundary conditions on the interface. This is the so-called Arbitrary Lagrangian–Eulerian (ALE) method[3] known for its great capability in resolving the flow and stress distributions accurately along the fluid-structure interface. However, for fluid-structure interaction (FSI) problems involving large displacements (which is the case here), the necessary time-consuming remeshing during the course of the simulation leads to a substantial computational costs. In addition, in applications with large deformations, the quality of the adapted grid and therefore the solution can suffer significantly. An alternative method to the body-fitted approach is the immersed boundary method (IBM). The IBM, originally introduced by Peskin,[4] found its initial application in simulating cardiac mechanics and the associated blood flow. Unlike the body-conforming approach, this method uses an overlapping (i.e., non-conforming) discretizations for the fluid and structural domains. Eulerian and Lagrangian frames of references are used to describe physical quantities associated with the fluid and the structure, respectively. The no-slip boundary condition is enforced on the fluid–solid interface by formulating an appropriate boundary forcing term.

Mittal and Iaccarino[5] classified the existing IBMs into two categories based on the way this forcing term is introduced into the governing equations. The first is termed as the *continuous forcing approach* in which the boundary forcing is incorporated into the continuous governing equations of the fluid flow (i.e., before discretization). This gives this class of IBMs the attractive feature of being able to formulate the forcing term independent of the employed spatial discretization. In the second class denoted the *discrete forcing approach*, the governing equations are first discretized without considering the IB. Then, its influence is brought up by adjusting the discretization in the cells in its vicinity. Although the formulated forcing term is intimately connected to the spatial discretization scheme, the discrete forcing enables a sharp representation of the IB. Examples of this class of IBMs employing a direct imposition of boundary conditions are the ghost-cell finite-difference approach[6] and the cut-cell finite-volume approach.[7] It is worth mentioning that this class of IBMs encounters the challenge of the "freshly cleared" cells when the boundary is moving. In simple terms, this issue arises when a spatial discontinuity linked to the sharp representation of the IB becomes apparent within fluid cells that were within the solid phase during the previous time step. Although remedies to this issue were suggested in Udaykumar, Mittal, and Shyy,[8] Udaykumar *et al.*,[9] this challenge is not met in the continuous forcing approach. This is due to the spreading effect across a few grid cells on both sides of the boundary, facilitating a gradual transition between the fluid and solid phases, effectively mitigating temporal discontinuities for cells transitioning into the fluid phase. Since this work is concerned with the inclusion of a moving IB (here the paddle) into the computational domain, continuous forcing IBMs are favored and discussed hereafter.

The first IBM with a continuous forcing approach is the original IBM.[4,10] At the continuous level, the boundary forces are represented by a source term added to the governing equations as singular functions acting along the immersed surface. At the discrete level, the IB is described by a set of Lagrangian markers conceived as material points and the boundary forces are localized at these discrete Lagrangian locations. In order to avoid numerical instabilities, these localized forces are introduced in conjunction with a regularized delta function of finite support, effectively spreading the force smoothly over the neighboring Eulerian cells. Depending on the material type of the IB (i.e., elastic or rigid), different methods were used to compute the forcing function. For flexible boundaries, Peskin[4,11] used Hooke's law to compute the IB forcing in the simulation of blood flow inside a heart with flexible valves. Different approaches were proposed for the incorporation of rigid immersed boundaries. Beyer and LeVeque[12] and Lai and Peskin[13] suggested to consider a structure attached to an equilibrium location by a spring of large stiffness. This formulation of the singular force is viewed as a specific version of the feedback mechanism outlined in the virtual boundary method, initially proposed by Goldstein, Handler, and Sirovich[14] and subsequently applied in Saiki and Biringen.[15] In this technique, forces (conceived as a system of virtual springs and dampers) are computed based on the difference between the actual and the desired values of the velocity. These are then set to act in an opposing manner to reinstate the desired velocity. This indirect formulation of the forces introduces user-defined (spring and damper) parameters that are chosen as a compromise between achieving acceptable boundary conditions and sufficiently large time step sizes.[13,16] To circumvent the drawback of the time step restriction associated with these indirect penalty formulations (also see Angot, Bruneau, and Fabrie,[17] Khadra *et al.*[18]), direct force formulations were proposed. Fadlun, Verzicco, and Orlandi[19] introduced a direct forcing scheme that alters the discretized momentum equation at Eulerian points in the proximity of the IB such that the desired velocity at the boundary points is attained. However, undesirable force oscillations in flows involving moving boundaries were observed due to the interpolation procedure relating values at fixed grid nodes and values at arbitrary located boundaries. Uhlmann[20] addressed this issue by refining an alternative direct forcing scheme. His approach relies on computing the force on the Lagrangian marker first and subsequently spreading it onto the neighboring Eulerian cells. This renders this method particularly well-suited for the intended application in this study. To enable the application of this method on a general, possibly curvilinear, non-uniform Eulerian grid without compromising either its conservation properties or the order of the underlying spatial discretization, it is employed according to the work proposed by Pinelli *et al.*[21]

The paper is organized as follows: Section II describes the experimental setup of the wind gust generator. The immersed boundary method used to simulate the flow in the gust generator is explained in Sec. III, while the numerical framework relying on the large-eddy simulation (LES) technique is detailed in Sec. IV. All details of the setup including the kinematics of the paddle are given in Sec. V. Starting with a general description of the arising flow field, a comparison of the measured and predicted velocity signals is presented in Sec. VI. Finally, the forces acting by the moving paddle on the flow are analyzed.

II. EXPERIMENTAL SETUP OF THE WIND GUST GENERATOR

Since one objective of the current study is to numerically mimic the novel wind gust generator (WGG) denoted the "*paddle*," in the following, the setup of the WGG is briefly described. The description is based on the work of Wood, Breuer, and Neumann[1] and Wood and Breuer.[22] The concept relies on the idea to design a device that allows to artificially generate horizontal wind gusts within a classical Göttingen-type wind tunnel. It should be possible to cost-efficiently retrofit the WGG to any wind tunnel with an open test section and to build it from standard components.

The working principle sketched in Fig. 1 is simple: Initially, the nozzle is fully open and the fluid flow from the left to the right between the nozzle and the receiver defines the measurement section in which the object of interest can be placed. The horizontal gust is generated by partially blocking the outlet of the wind tunnel nozzle by the paddle. For this purpose, a rigid aluminum plate (red) is screwed onto the movable saddle of a tooth belt axis. That is clamped onto a massive rig and positioned above the outlet of the nozzle. The saddle is powered by a servo motor, a gear box, and an axial kit (Festo). All relevant kinematic parameters (stroke length, velocity, and acceleration) of the tooth belt axis can be fully controlled by the software tool `Festo Automation Suite`.

The starting point is the situation when the wind tunnel is operating in its normal mode. Then, the paddle of the WGG is set into motion, moving vertically downward into the free-stream. By reducing the outlet area, the flow is strongly accelerated underneath the moving paddle leading to the unsteady flow velocity. The maximum velocity of the artificially generated horizontal gust is approximately achieved at the time when the paddle reaches its maximum displacement and thus the maximum blocking of the nozzle. After this instant in time, the plate is set to move back upward causing an expansion of the flow. Consequently, the flow velocity decreases again and after a transition period the free-stream velocity is recovered. Since the movement of the paddle can be arbitrary defined by the distance it covers, its velocity and acceleration during the downward and upward stroke, the gust can be set as desired within certain limits. In Wood, Breuer, and Neumann,[1] five different motion patterns of the paddle were investigated, and their effects on the generated gusts were analyzed. For gust type 1 relying on a fast and symmetric motion pattern, the parameters are set to mimic the 1-cosine gust shape considered by the IEC-Standard[23] and denoted as Extreme Coherent Gust (ECG). This case is considered in the present study.

III. IMMERSED BOUNDARY METHOD WITH A DIRECT FORCING APPROACH

In this work, the paddle is modeled as a moving boundary employing the immersed boundary (IB) method with a direct forcing approach proposed by Uhlmann.[20] On the continuous level, the presence of the immersed boundary (Γ) is incorporated into the continuous governing equations by the addition of a forcing term $\mathbf{f}$ to their right-hand side. The Navier–Stokes equations for an incompressible fluid on the domain Ω then read

$$\left.\begin{aligned} \rho\,\frac{\partial \mathbf{u}}{\partial t} &= \rho\,\nabla\cdot(\mathbf{u}\mathbf{u}) + \mu\Delta\mathbf{u} - \nabla p + \mathbf{f} \\ \nabla\cdot\mathbf{u} &= 0 \end{aligned}\right\} \quad \mathbf{x}\in\Omega, \tag{1}$$

where $\mathbf{f}$ is a volume force that represents the influence of the solid object on the surrounding fluid. On the discrete level, quantities at the Eulerian (i.e., fluid grid) and the Lagrangian (i.e., solid's boundary points) locations are distinguished by lower- and upper-case letters, respectively. In the scope of the collocated grid arrangement employed in the finite-volume solver used, Eulerian locations refer to the cell centers $\mathbf{x}_{i,j,k}$. The Lagrangian locations $\mathbf{X}_l$ are the coordinates of the distributed Lagrangian force points defining the immersed boundary Γ

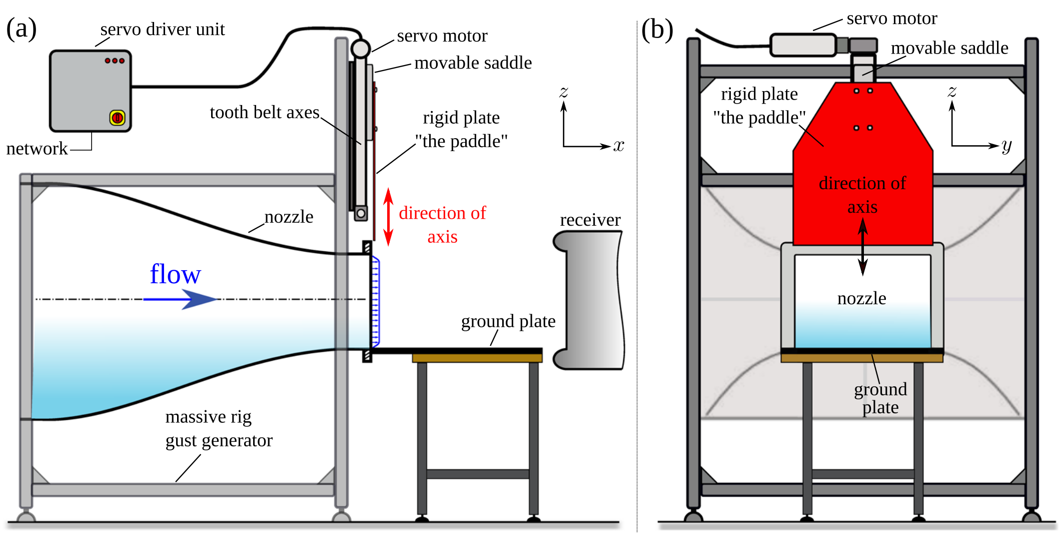

FIG. 1. Experimental setup of the wind tunnel with the new wind gust generator: (a) side view showing the test section with the additional ground plate and (b) front view depicting the paddle and the outlet of the nozzle. Reprinted with permission from Wood *et al.*, J. Wind Eng. Ind. Aerodyn. **230**, 105170 (2022). Copyright 2022 Author(s), licensed under a Creative Commons Attribution (CC BY) license.

(i.e., $\mathbf{X}_l \in \Gamma \, \forall \, 1 \leq l \leq N_L$, where N_L denotes the total number of Lagrangian markers).

The following describes the formulation of the volume force adopted in the framework of the predictor–corrector method used to solve the Navier–Stokes equations. The predictor step consists of explicitly marching the solution in time to obtain an intermediate velocity $\mathbf{u}^*$. To keep the description compact, the procedure is explained based on the simple explicit Euler scheme. The final formulation relies on a three-substeps low-storage Runge–Kutta scheme of second-order accuracy

$$\rho \, \frac{\mathbf{u}^* - \mathbf{u}^n}{\Delta t} = \mathbf{rhs}^n. \tag{2}$$

Here, $\mathbf{rhs}^n$ is a short-hand for the summation of the convective, diffusive, and pressure terms at time step t^n. When considering the immersed boundary force term appearing in Eq. (1), Eq. (2) becomes

$$\rho \, \frac{\mathbf{u}^* - \mathbf{u}^n}{\Delta t} = \mathbf{rhs}^n + \mathbf{f}^n. \tag{3}$$

One way to find the force $\mathbf{f}^n$ that would directly set the intermediate velocity to the desired velocity $\mathbf{u}_d$ on the fluid–solid interface is to simply write

$$\mathbf{f}^n = \rho \, \frac{\mathbf{u}_d - \mathbf{u}^n}{\Delta t} - \mathbf{rhs}^n. \tag{4}$$

However, this will only hold true if the Eulerian and Lagrangian locations are coincident. When dealing with time-dependent immersed boundaries, it is often the case that the fluid–solid interface is not conforming to the cell centers of the fluid grid. Here, the distinction previously made between the Eulerian and Lagrangian positions becomes necessary.

Fadlun, Verzicco, and Orlandi[19] suggested three interpolation procedures with an ascending order of accuracy when this direct forcing approach is used. The first is to assign the force in Eq. (4) to all Eulerian points closest to the immersed boundary as if they are coincident to it. This results in a diffused interface rather than a sharp one. The second interpolation procedure is an improved version of the first, where a volume-fraction weighting is considered to scale the forcing applied to the momentum cells closest to the boundary. The last proposition is to linearly interpolate the velocity of the immersed boundary $\mathbf{u}_d$ to the Eulerian points closest to the boundary to obtain $\bar{\mathbf{u}}_d$ and substitute it in Eq. (4) instead of $\mathbf{u}_d$. However, Uhlmann[20] reported that the use of this direct forcing approach might cause serious oscillations of the hydrodynamic forces due to inadequate smoothing.

In the direct forcing scheme proposed by Uhlmann,[20] the force term is evaluated at the Lagrangian force points instead

$$\mathbf{F}^n = \rho \, \frac{\mathbf{U}_d - \mathbf{U}^n}{\Delta t} - \mathbf{RHS}^n \quad \forall \quad \mathbf{X}_l, \tag{5}$$

with $\mathbf{U}_d$ being the velocity at the fluid–solid interface. This velocity is to be explicitly prescribed by the rigid-body motion of the moving paddle considered in this work. In Eq. (5), the two unknown terms (i.e., $\mathbf{U}^n$ and $\mathbf{RHS}^n$) can both be combined into a single unknown, namely, the intermediate velocity $\mathbf{U}^*$ at a Lagrangian location

$$\mathbf{U}^* = \mathbf{U}^n + \frac{\Delta t}{\rho} \mathbf{RHS}^n. \tag{6}$$

An Eulerian analogue to Eq. (6) exists in the projection method used in this work [by solving Eq. (2) for $\mathbf{u}^*$]. Thus, by solving Eq. (6) for $\mathbf{U}^n$ and substituting it into Eq. (5), the following expression of the Lagrangian force results:

$$\mathbf{F}^n = \rho \, \frac{\mathbf{U}_d - \mathbf{U}^*}{\Delta t} \quad \forall \quad \mathbf{X}_l. \tag{7}$$

In order to couple the fluid and the solid phases, one has to conveniently transfer quantities between the two frames of reference. Therefore, the original IB method introduced by Peskin[10] depending on the use of a bounded continuous approximation of the Dirac delta function δ_h (also referred to as the regularized delta function) is employed. The transfer equations for a uniform Cartesian grid g_h of grid size h read

$$\mathbf{U}^*(\mathbf{X}_l) = \sum_{i,j,k \in g_h} \mathbf{u}^*(\mathbf{x}_{i,j,k}) \, \delta_h(\mathbf{x}_{i,j,k} - \mathbf{X}_l) \Delta v_{i,j,k} \quad \forall \, 1 \leq l \leq N_L, \tag{8}$$

$$\mathbf{f}(\mathbf{x}_{i,j,k}) = \sum_{l=1}^{N_L} \mathbf{F}(\mathbf{X}_l) \, \delta_h(\mathbf{x}_{i,j,k} - \mathbf{X}_l) \Delta V_l \quad \forall \, \mathbf{x}_{i,j,k} \in g_h, \tag{9}$$

where $\Delta v_{i,j,k}$ is the volume of the Eulerian cell (i, j, k), and ΔV_l is the volume associated with the Lagrangian force point (l). The operation performed by Eq. (8) is called the interpolation operation $\mathcal{I}(\mathbf{u}^*)$, owing to the fact that it computes a Lagrangian quantity as a weighted average of the neighboring Eulerian quantities [see Fig. 2(a)]. Contrarily, Eq. (9) is referred to as the spreading operation $\mathcal{S}(\mathbf{F})$, where the force is spread out from a Lagrangian force point to the Eulerian points in its vicinity [see Fig. 2(b)]. Hence, the steps of the predictor–corrector method accounting for the immersed boundary can be summarized by the following equations:

$$1.\ \mathbf{u}^* = \mathbf{u}^n + \frac{\Delta t}{\rho} \mathbf{rhs}^n \quad \forall \, \mathbf{x}_{i,j,k} \in g_h, \tag{10}$$

$$2.\ \mathbf{U}^* = \mathcal{I}(\mathbf{u}^*) \quad \forall \, \mathbf{X}_l \in \Gamma, \tag{11}$$

$$3.\ \mathbf{F} = \rho \, \frac{\mathbf{U}_d - \mathbf{U}^*}{\Delta t} \quad \forall \, \mathbf{X}_l \in \Gamma, \tag{12}$$

$$4.\ \mathbf{f} = \mathcal{S}(\mathbf{F}) \quad \forall \, \mathbf{x}_{i,j,k} \in g_h, \tag{13}$$

$$5.\ \mathbf{u}^{**} = \mathbf{u}^* + \frac{\Delta t}{\rho} \mathbf{f} \quad \forall \, \mathbf{x}_{i,j,k} \in g_h, \tag{14}$$

$$6.\ \Delta p' = \frac{\rho}{\Delta t} \nabla \cdot \mathbf{u}^{**} \quad \forall \, \mathbf{x}_{i,j,k} \in g_h, \tag{15}$$

$$7.\ \mathbf{u}^{n+1} = \mathbf{u}^n - \frac{\Delta t}{\rho} \nabla p' \quad \forall \, \mathbf{x}_{i,j,k} \in g_h. \tag{16}$$

Compared to a classic predictor–corrector scheme, steps 2 to 5 have been added and lead to a second intermediate velocity $\mathbf{u}^{**}$. That builds the basis for the right-hand side of the Poisson equation (15) for the pressure correction p' (step 6) and the final determination of the new velocity $\mathbf{u}^{n+1}$ (step 7).

The regularized delta function considered is that defined by Roma, Peskin, and Berger[24] (see Fig. 3), and it involves three grid points in each coordinate direction

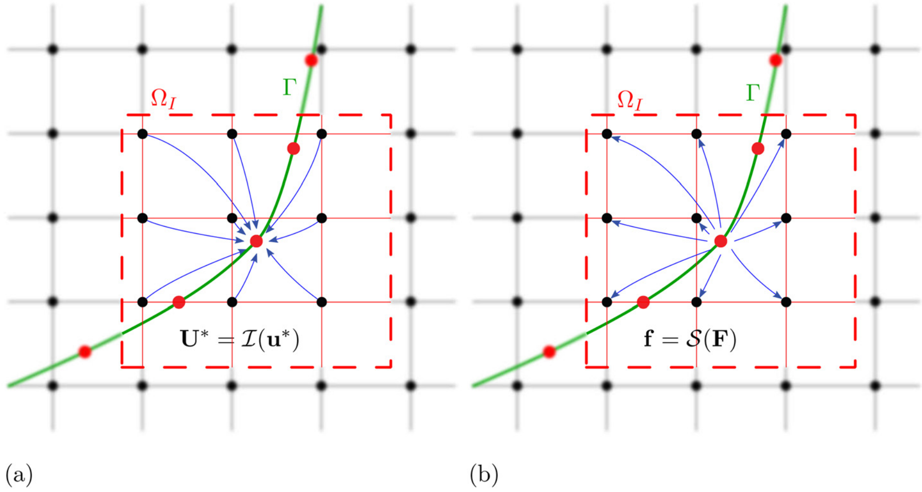

FIG. 2. (a) Interpolation of Eulerian velocities and (b) spreading of a Lagrangian force.

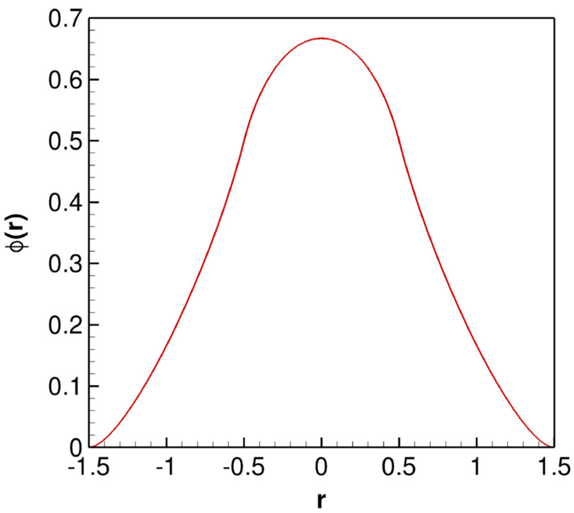

FIG. 3. Regularized delta function by Roma, Peskin, and Berger.[24]

$$\delta_d(r) = \frac{1}{d}\,\phi_d(r)$$
$$= \frac{1}{d}\begin{cases} \dfrac{1}{3}\left(1+\sqrt{-3r^2+1}\right), & \text{if } |r| \le \dfrac{1}{2}, \\ \dfrac{1}{6}\left(5-3|r|-\sqrt{-3(1-|r|)^2+1}\right), & \text{if } \dfrac{1}{2} \le |r| \le \dfrac{3}{2}, \\ 0, & \text{otherwise}, \end{cases} \tag{17}$$

where the subscript d is the dilation parameter ($d = h$ for uniform grids). It defines the dimensions of the kernel's support Ω_I, and the parameter r is the distance between an Eulerian and a Lagrangian coordinate normalized by the dilation parameter [$r = (x - X)/d$].

The smoothing kernel is continuous, of compact support, and designed to satisfy a set of discrete moment conditions (the zeroth and first moments)

$$\sum_{i,j,k \in g_h} \delta_h(\mathbf{x}_{i,j,k} - \mathbf{X}_l)\Delta v_{i,j,k} = 1, \tag{18}$$

$$\sum_{i,j,k \in g_h} (\mathbf{x}_{i,j,k} - \mathbf{X}_l)\delta_h(\mathbf{x}_{i,j,k} - \mathbf{X}_l)\Delta v_{i,j,k} = 0. \tag{19}$$

These discrete analogues of the basic properties of the Dirac delta function ensure the integral conservation of the force and moment in the spreading operation

$$\begin{aligned}\sum_{i,j,k \in g_h} \mathbf{f}(\mathbf{x}_{i,j,k})\Delta v_{i,j,k} &= \sum_{l=1}^{N_L} \mathbf{F}(\mathbf{X}_l)\cancelto{1}{\left(\sum_{i,j,k \in g_h} \delta_h(\mathbf{x}_{i,j,k} - \mathbf{X}_l)\Delta v_{i,j,k}\right)}\Delta V_l \\ &= \sum_{l=1}^{N_L} \mathbf{F}(\mathbf{X}_l)\Delta V_l, \end{aligned} \tag{20}$$

$$\begin{aligned}&\sum_{i,j,k \in g_h} \mathbf{x}_{i,j,k} \times \mathbf{f}(\mathbf{x}_{i,j,k})\Delta v_{i,j,k} \\ &= \sum_{l=1}^{N_L} \cancelto{\mathbf{X}_l}{\left(\sum_{i,j,k \in g_h} \mathbf{x}_{i,j,k}\delta_h(\mathbf{x}_{i,j,k} - \mathbf{X}_l)\Delta v_{i,j,k}\right)} \times \mathbf{F}(\mathbf{X}_l)\Delta V_l \\ &= \sum_{l=1}^{N_L} \mathbf{X}_l \times \mathbf{F}(\mathbf{X}_l)\Delta V_l. \end{aligned} \tag{21}$$

The wind tunnel geometry simulated in this work requires a stretched grid that clusters the grid points close to walls in order to accurately capture the boundary layer. The grid is therefore Cartesian non-uniform. For the sake of writing the equations in a compact manner, in the following, the shift between an Eulerian and a Lagrangian coordinate (e.g., $x - X$) shall be referred to by the subscript "s" (i.e., $x_s = x - X$, $y_s = y - Y$, and $z_s = z - Z$).

In 1 D, the non-uniformity of the grid is accounted for by defining a modified window function according to Pinelli *et al.*[21]

$$\tilde{\delta}_d(x_s) = \sum_{l=1}^{n} b_l(X, d)\, x_s^{(l-1)}\, \delta_d(x_s), \tag{22}$$

where $b_l(X, d)$ are the unknown polynomial coefficients, and their number n is to be defined later. The unknown polynomial coefficients are determined by imposing a set of modified moment conditions

$$\tilde{m}_{(i-1)}(X) = \int_{\Omega_l} x_s^{(i-1)}\, \tilde{\delta}_d(x_s)\, dx = \delta_{i1}, \tag{23}$$

where δ_{ij} is the Kronecker delta. By substituting Eq. (22) in Eq. (23), one can write the modified moment conditions in terms of the original moments

$$\begin{aligned}\tilde{m}_{(i-1)}(X) &= \int_{\Omega_l} x_s^{(i-1)} \sum_{l=1}^{n} b_l(X,d)\, x_s^{(l-1)}\, \delta_d(x_s)\, dx \\ &= \sum_{l=1}^{n} b_l(X,d) \int_{\Omega_l} x_s^{(i+l-2)}\, \delta_d(x_s)\, dx \\ &= \sum_{l=1}^{n} b_l(X,d)\, m_{(i+l-2)}(X) = \delta_{i1}.\end{aligned} \tag{24}$$

The number of the required polynomial coefficients in Eq. (22) (i.e., n) primarily depends on the required number of the reproducing moment conditions to be satisfied, the dimensionality of the problem, and the order of the underlying Eulerian spatial discretization scheme.[21] In 3 D, the linear combinations of $\{1, x, y, z\}$ guarantees the integral conservation of the force and moment [i.e., Eqs. (20) and (21)]. Since the governing equations are discretized in space by a second-order accurate scheme (i.e., surface and volume integrals are approximated by the midpoint rule), the modified window function then reads

$$\begin{aligned}\tilde{\delta}_{\xi,\eta,\zeta}(x_s,y_s,z_s) = \Big[&b_1 + b_2\, x_s + b_3\, y_s + b_4\, z_s \\ &+ b_5\,(x_s\, y_s) + b_6\,(y_s\, z_s) + b_7\,(z_s\, x_s) \\ &+ b_8\, x_s^2 + b_9\, y_s^2 + b_{10}\, z_s^2\Big]\, \delta_{\xi,\eta,\zeta}(x_s,y_s,z_s),\end{aligned} \tag{25}$$

where the dependency of the coefficients can be expressed by $b_l = b_l(X, Y, Z, \xi, \eta, \zeta)$, $l = 1, \ldots, 10$, and the original window function is defined as the product

$$\delta_{\xi,\eta,\zeta}(x_s,y_s,z_s) = \delta_\xi(x_s,y_s,z_s)\, \delta_\eta(x_s,y_s,z_s)\, \delta_\zeta(x_s,y_s,z_s), \tag{26}$$

with the subscripts ξ, η, and ζ being the dilatation parameters in each coordinate direction. Hence, 10 modified moment conditions need to be satisfied in order to evaluate the unknown polynomial coefficients. The continuous form of these conditions read

$$\begin{aligned}&\tilde{m}_{\mathbf{i}(h),\mathbf{j}(h),\mathbf{k}(h)}(X,Y,Z) \\ &= \int_{\Omega_l} x_s^{\mathbf{i}(h)}\, y_s^{\mathbf{j}(h)}\, z_s^{\mathbf{k}(h)} \sum_{l=1}^{n=10} b_l\, x_s^{\mathbf{i}(l)}\, y_s^{\mathbf{j}(l)}\, z_s^{\mathbf{k}(l)}\, \delta_{\xi,\eta,\zeta}(x_s,y_s,z_s)\, dx\, dy\, dz = \delta_{h1},\end{aligned} \tag{27}$$

where the arguments $h, l = 1, \ldots, 10$ and the vectors $\mathbf{i}$, $\mathbf{j}$, and $\mathbf{k}$ are defined in such a way that the coordinate shifts (x_s, y_s and z_s) within the summation are raised to their respective powers according to Eq. (25)

$$\mathbf{i} = [0,\ 1,\ 0,\ 0,\ 1,\ 0,\ 1,\ 2,\ 0,\ 0], \tag{28}$$

$$\mathbf{j} = [0,\ 0,\ 1,\ 0,\ 1,\ 1,\ 0,\ 0,\ 2,\ 0], \tag{29}$$

$$\mathbf{k} = [0,\ 0,\ 0,\ 1,\ 0,\ 1,\ 1,\ 0,\ 0,\ 2]. \tag{30}$$

Further simplification yields

$$\begin{aligned}&\tilde{m}_{\mathbf{i}(h),\mathbf{j}(h),\mathbf{k}(h)}(X,Y,Z) \\ &= \sum_{l=1}^{n=10} b_l \int_{\Omega_l} x_s^{\mathbf{i}(h)+\mathbf{i}(l)}\, y_s^{\mathbf{j}(h)+\mathbf{j}(l)}\, z_s^{\mathbf{k}(h)+\mathbf{k}(l)}\, \delta_{\xi,\eta,\zeta}(x_s,y_s,z_s)\, dx\, dy\, dz \\ &= \sum_{l=1}^{n=10} b_l\, m_{\mathbf{i}(h)+\mathbf{i}(l),\mathbf{j}(h)+\mathbf{j}(l),\mathbf{k}(h)+\mathbf{k}(l)}(X,Y,Z) = \delta_{h1}.\end{aligned} \tag{31}$$

Letting h and l refer to the row and column number, respectively, the resulting symmetric linear system of equations that needs to be solved for each Lagrangian location reads

$$\begin{bmatrix}\tilde{m}_{0,0,0}\\ \tilde{m}_{1,0,0}\\ \tilde{m}_{0,1,0}\\ \tilde{m}_{0,0,1}\\ \tilde{m}_{1,1,0}\\ \tilde{m}_{0,1,1}\\ \tilde{m}_{1,0,1}\\ \tilde{m}_{2,0,0}\\ \tilde{m}_{0,2,0}\\ \tilde{m}_{0,0,2}\end{bmatrix}
\begin{bmatrix}
m_{0,0,0} & m_{1,0,0} & m_{0,1,0} & m_{0,0,1} & m_{1,1,0} & m_{0,1,1} & m_{1,0,1} & m_{2,0,0} & m_{0,2,0} & m_{0,0,2}\\
 & m_{2,0,0} & m_{1,1,0} & m_{1,0,1} & m_{2,1,0} & m_{1,1,1} & m_{2,0,1} & m_{3,0,0} & m_{1,2,0} & m_{1,0,2}\\
 & & m_{0,2,0} & m_{0,1,1} & m_{1,2,0} & m_{0,2,1} & m_{1,1,1} & m_{2,1,0} & m_{0,3,0} & m_{0,1,2}\\
 & & & m_{0,0,2} & m_{1,1,1} & m_{0,1,2} & m_{1,0,2} & m_{2,0,1} & m_{0,2,1} & m_{0,0,3}\\
 & & & & m_{2,2,0} & m_{1,2,1} & m_{2,1,1} & m_{3,1,0} & m_{1,3,0} & m_{1,1,2}\\
 & & & & & m_{0,2,2} & m_{1,1,2} & m_{2,1,1} & m_{0,3,1} & m_{0,1,3}\\
 & & & & & & m_{2,0,2} & m_{3,0,1} & m_{1,2,1} & m_{1,0,3}\\
 & & & & & & & m_{4,0,0} & m_{2,2,0} & m_{2,0,2}\\
 & & & & & & & & m_{0,4,0} & m_{0,2,2}\\
 symm. & & & & & & & & & m_{0,0,4}
\end{bmatrix}
\begin{bmatrix}b_1\\ b_2\\ b_3\\ b_4\\ b_5\\ b_6\\ b_7\\ b_8\\ b_9\\ b_{10}\end{bmatrix}
=
\begin{bmatrix}1\\0\\0\\0\\0\\0\\0\\0\\0\\0\end{bmatrix}. \tag{32}$$

The entries of the symmetric matrix are numerically evaluated for each Lagrangian marker $\mathbf{X} = (X, Y, Z)$ by transforming the integral in Eq. (31) to a summation over the Eulerian cells falling within the cage $\Omega_l(\xi, \eta, \zeta)$. First, the closest cell center $\mathbf{x}_{\hat{i},\hat{j},\hat{k}} = (x_{\hat{i},\hat{j},\hat{k}},\ y_{\hat{i},\hat{j},\hat{k}},\ z_{\hat{i},\hat{j},\hat{k}})$ is sought, and two of its neighbors in each direction are identified (i.e., $\mathcal{S}_I = \{\mathbf{x}_{\hat{i}+l,\hat{j}+l,\hat{k}+l}\}$ for $l = -1, 0, 1$). Maximum and minimum local grid spacings in each direction are then evaluated according to Pinelli *et al.*[21]

$$\begin{aligned} h_x^+(\mathbf{X}) &= \max\{|x_{i,j,k} - x_{i-1,j,k}|\}, x_{i,j,k}, x_{i-1,j,k} \in \mathcal{S}_I, \\ h_x^-(\mathbf{X}) &= \min\{|x_{i,j,k} - x_{i-1,j,k}|\}, x_{i,j,k}, x_{i-1,j,k} \in \mathcal{S}_I, \\ h_y^+(\mathbf{X}) &= \max\{|y_{i,j,k} - y_{i,j-1,k}|\}, y_{i,j,k}, y_{i,j-1,k} \in \mathcal{S}_I, \\ h_y^-(\mathbf{X}) &= \min\{|y_{i,j,k} - y_{i,j-1,k}|\}, y_{i,j,k}, y_{i,j-1,k} \in \mathcal{S}_I, \\ h_z^+(\mathbf{X}) &= \max\{|z_{i,j,k} - z_{i,j,k-1}|\}, z_{i,j,k}, z_{i,j,k-1} \in \mathcal{S}_I, \\ h_z^-(\mathbf{X}) &= \min\{|z_{i,j,k} - z_{i,j,k-1}|\}, z_{i,j,k}, z_{i,j,k-1} \in \mathcal{S}_I, \end{aligned} \tag{33}$$

and the dilation parameters depending on the local grid spacing are defined as

$$\xi_I = \frac{5}{6}\, h_x^+(\mathbf{X}) + \frac{1}{6}\, h_x^-(\mathbf{X}), \tag{34}$$

$$\eta_I = \frac{5}{6}\, h_y^+(\mathbf{X}) + \frac{1}{6}\, h_y^-(\mathbf{X}), \tag{35}$$

$$\zeta_I = \frac{5}{6}\, h_z^+(\mathbf{X}) + \frac{1}{6}\, h_z^-(\mathbf{X}). \tag{36}$$

The discrete counterpart of the matrix entries can now be written as

$$m_{i,j,k}(X,Y,Z) = \sum_{h,l,q\in\mathcal{S}_I} (x_{h,l,q} - X)^i (y_{h,l,q} - Y)^j (z_{h,l,q} - Z)^k\, \delta_{\xi_I,\eta_I,\zeta_I}(x_s, y_s, z_s)\, \Delta v_{h,l,q}. \tag{37}$$

The symmetric linear system of equations [i.e., Eq. (32)] is solved using the "dsysv" subroutine provided by the linear algebra package LAPACK.[25]

IV. NUMERICAL FRAMEWORK

A. Flow solver

The present study employs the in-house Navier–Stokes solver FASTEST-3D[26] to solve for the incompressible fluid flow. The governing equations are discretized in space using the finite-volume technique on a curvilinear, block-structured body-fitted grid with a collocated cell-centered variable arrangement. Parallelization is achieved by domain decomposition and explicit message passing based on the Message Passing Interface (MPI). The midpoint rule is used to approximate the surface and volume integrals and the required flow variables at cell faces are linearly interpolated from neighboring cell-centered values leading to a second-order spatial accuracy. The convective fluxes are approximated using the flux blending technique,[27,28] combining 3% of a first-order accurate upwind scheme with 97% of a second-order accurate central scheme. To avoid pressure field oscillations, the momentum interpolation technique of Rhie and Chow[29] is employed for non-staggered grids to couple the pressure and velocity fields.

For the pressure–velocity coupling problem, a semi-implicit predictor–corrector scheme[30] with second-order accuracy is used. The momentum equations are first advanced in time using a low-storage multi-stage Runge–Kutta method to obtain an intermediate velocity. This velocity is known for not satisfying the continuity equation (i.e., not a solenoidal vector field). The corrector step then ensures mass conservation by solving a Poisson equation for the pressure correction (here through an incomplete lower–upper (LU) decomposition method[31]) and projecting the coupled flow variables (i.e., velocities and pressure) to the space of divergence-free vector fields. This procedure provides second-order accuracy in both space and time. The large-eddy simulation (LES) technique is used to only resolve the large-scale turbulent flow field and model the small scales by a subgrid-scale (SGS) model. The standard Smagorinsky SGS model[32] with the well-established constant $C_S = 0.1$ and van-Driest damping near solid walls is applied. Since the near-wall grid resolution is sufficient to resolve the viscous sublayer as will be shown in Sec. V, wall functions are not required. Instead, wall-resolved LES is carried out. To incorporate the immersed boundary method, steps 2 to 5 described in Sec. III are additionally carried out.

B. Lagrangian marker tracking

The tracking of the Lagrangian markers is performed in the computational space (c-space) obtained by transforming the structured grid connecting the cell centers [i.e., **z**-grid in Fig. 4(a)] to an orthonormal grid. The time-consuming search process in the physical space (p-space) associated with finding the new computational cell containing the Lagrangian marker can therefore be avoided. The location of the Lagrangian marker in the c-space $\boldsymbol{\xi}_l$ [see Fig. 4(b)] is defined as the summation of the index triple of the cell containing it and a fractional offset as

$$\boldsymbol{\xi}_l = [\xi_l, \eta_l, \zeta_l] = [i_l, j_l, k_l] + \left[\Delta\xi_l^+, \Delta\eta_l^+, \Delta\zeta_l^+\right]. \tag{38}$$

The use of such a definition is also advantageous for the efficient search of the nearest cell center to the Lagrangian marker required for defining the bounds of the regularized delta function (i.e., for finding $\mathbf{x}_{\hat{i},\hat{j},\hat{k}}$). The index triples $[i_l, j_l, k_l]$ and $[\hat{i}_l, \hat{j}_l, \hat{k}_l]$ can be obtained by applying the integer operators "int" and "nint" provided by programming languages on the computational coordinates $[\xi_l, \eta_l, \zeta_l]$, respectively. The fractional offset can be solved for using Eq. (38) and its complement thereafter reads

$$\Delta\xi_l^- = 1 - \Delta\xi_l^+, \quad \Delta\eta_l^- = 1 - \Delta\eta_l^+, \quad \Delta\zeta_l^- = 1 - \Delta\zeta_l^+. \tag{39}$$

The fractional offset and its complement can be employed to write the transformation T of the marker's position $\boldsymbol{\xi}_l$ to the p-space by means of the trilinear interpolation using the cell centered values $\mathbf{x}_{i,j,k}$[33]

$$\begin{aligned} \mathbf{X}_l = T(\boldsymbol{\xi}_l) = {}& \mathbf{x}_{i,j,k}[\Delta\xi_l^-\Delta\eta_l^-\Delta\zeta_l^-] + \mathbf{x}_{i+1,j,k}\left[\Delta\xi_l^+\Delta\eta_l^-\Delta\zeta_l^-\right] \\ & + \mathbf{x}_{i,j+1,k}\left[\Delta\xi_l^-\Delta\eta_l^+\Delta\zeta_l^-\right] + \mathbf{x}_{i,j,k+1}\left[\Delta\xi_l^-\Delta\eta_l^-\Delta\zeta_l^+\right] \\ & + \mathbf{x}_{i+1,j+1,k}\left[\Delta\xi_l^+\Delta\eta_l^+\Delta\zeta_l^-\right] + \mathbf{x}_{i+1,j,k+1}\left[\Delta\xi_l^+\Delta\eta_l^-\Delta\zeta_l^+\right] \\ & + \mathbf{x}_{i,j+1,k+1}\left[\Delta\xi_l^-\Delta\eta_l^+\Delta\zeta_l^+\right] + \mathbf{x}_{i+1,j+1,k+1}\left[\Delta\xi_l^+\Delta\eta_l^+\Delta\zeta_l^+\right]. \end{aligned} \tag{40}$$

In addition to the visualization purpose of the immersed boundary, this interpolation is used to evaluate the Lagrangian location in physical coordinates required in Eqs. (8) and (9).

As previously mentioned in Sec. III, the immersed boundary (i.e., the paddle) is set into motion by a prescribed velocity $\mathbf{U}_d(t) = [U_d, V_d, W_d]$. This velocity is of course defined with respect to the p-space. In order to update the marker's location in the c-space, one

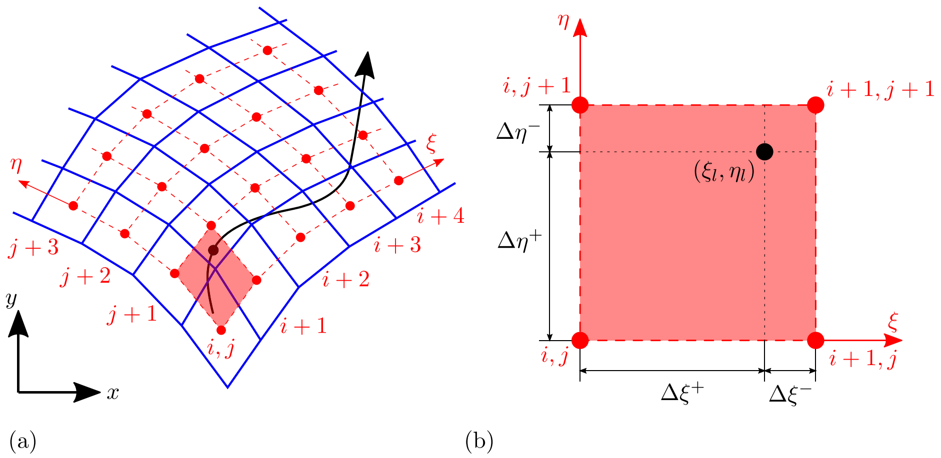

FIG. 4. (a) Two-dimensional p-space schematic sketch showing a computational grid (blue solid lines), cell centers (red circles), **z**-grid (red dashed lines), and Lagrangian marker's trajectory (black solid line) and (b) corresponding c-space representation showing the coefficients of the trilinear interpolation.

has to first transform the prescribed velocity components to the c-space by

$$\frac{d\xi_l}{dt} = \left(\frac{\partial\xi}{\partial x}\right)_l U_d + \left(\frac{\partial\xi}{\partial y}\right)_l V_d + \left(\frac{\partial\xi}{\partial z}\right)_l W_d, \tag{41}$$

$$\frac{d\eta_l}{dt} = \left(\frac{\partial\eta}{\partial x}\right)_l U_d + \left(\frac{\partial\eta}{\partial y}\right)_l V_d + \left(\frac{\partial\eta}{\partial z}\right)_l W_d, \tag{42}$$

$$\frac{d\zeta_l}{dt} = \left(\frac{\partial\zeta}{\partial x}\right)_l U_d + \left(\frac{\partial\zeta}{\partial y}\right)_l V_d + \left(\frac{\partial\zeta}{\partial z}\right)_l W_d. \tag{43}$$

Hence, the location of a Lagrangian marker is updated by carrying out the temporal integration

$$\xi_l^{n+1} = \xi_l^n + \left(\frac{\partial\xi}{\partial x}\right)_l \int_{t^n}^{t^{n+1}} U_d\,dt + \left(\frac{\partial\xi}{\partial y}\right)_l \int_{t^n}^{t^{n+1}} V_d\,dt + \left(\frac{\partial\xi}{\partial z}\right)_l \int_{t^n}^{t^{n+1}} W_d\,dt, \tag{44}$$

$$\eta_l^{n+1} = \eta_l^n + \left(\frac{\partial\eta}{\partial x}\right)_l \int_{t^n}^{t^{n+1}} U_d\,dt + \left(\frac{\partial\eta}{\partial y}\right)_l \int_{t^n}^{t^{n+1}} V_d\,dt + \left(\frac{\partial\eta}{\partial z}\right)_l \int_{t^n}^{t^{n+1}} W_d\,dt, \tag{45}$$

$$\zeta_l^{n+1} = \zeta_l^n + \left(\frac{\partial\zeta}{\partial x}\right)_l \int_{t^n}^{t^{n+1}} U_d\,dt + \left(\frac{\partial\zeta}{\partial y}\right)_l \int_{t^n}^{t^{n+1}} V_d\,dt + \left(\frac{\partial\zeta}{\partial z}\right)_l \int_{t^n}^{t^{n+1}} W_d\,dt. \tag{46}$$

The time-independent spatial metric coefficients (here for a fixed grid) appearing in Eqs. (44)–(46) are the entries of the Jacobian of the p-space to the c-space coordinate transformation $\mathbf{J}$ and are evaluated at the Lagrangian location. For this purpose, the *CZ*+ tracking scheme proposed by Schäfer and Breuer[33] is employed. First, the Jacobian of the inverse coordinate transformation $\mathbf{J}^{-1}$ (i.e., c-space to p-space) is analytically evaluated by differentiating Eq. (40). The first column of $\mathbf{J}^{-1}$ at a position $\boldsymbol{\xi}_l$ reads

$$\begin{aligned} \mathbf{J}_1^{-1}(\boldsymbol{\xi}_l) = \frac{\partial \mathbf{X}_l}{\partial \xi_1} = \frac{\partial T(\boldsymbol{\xi}_l)}{\partial \xi_1} = {} & \Delta\eta_l^- \Delta\zeta_l^- (\mathbf{x}_{i+1,j,k} - \mathbf{x}_{i,j,k}) \\ & + \Delta\eta_l^+ \Delta\zeta_l^- (\mathbf{x}_{i+1,j+1,k} - \mathbf{x}_{i,j+1,k}) \\ & + \Delta\eta_l^- \Delta\zeta_l^+ (\mathbf{x}_{i+1,j,k+1} - \mathbf{x}_{i,j,k+1}) \\ & + \Delta\eta_l^+ \Delta\zeta_l^+ (\mathbf{x}_{i+1,j+1,k+1} - \mathbf{x}_{i,j+1,k+1}). \end{aligned} \tag{47}$$

Following the evaluation of $\mathbf{J}_m^{-1}(\boldsymbol{\xi}_l)$ where $m = 1$, 2, and 3 and inverting it, the spatial metrics in Eqs. (44)–(46) are obtained.

V. DESCRIPTION OF THE SETUP

The aim of the present setup is to create a numerical counterpart of the experimental wind gust generator of Wood, Breuer, and Neumann[1] (i.e., the paddle). This shall facilitate a deeper analysis of the complex flow generated by the paddle as all flow field variables (i.e., velocities and pressure) are solved for throughout the entire computational domain. The complex wind tunnel geometry depicted in Fig. 1 is simplified to model the nozzle, the ground plate and the moving paddle as shown in Fig. 5. The geometry of the nozzle of the wind tunnel is simplified by neglecting its contraction ratio. It is replaced by a duct of length $l = 1.5$ m but with a rectangular cross-section which is identical to the outlet of the nozzle in the experimental setup ($h = 0.375$ m and $w = 0.5$ m). A uniform horizontal velocity field of $u_{inlet}^{steady} = 4.914$ m/s is defined at the inlet patch. The flow and especially

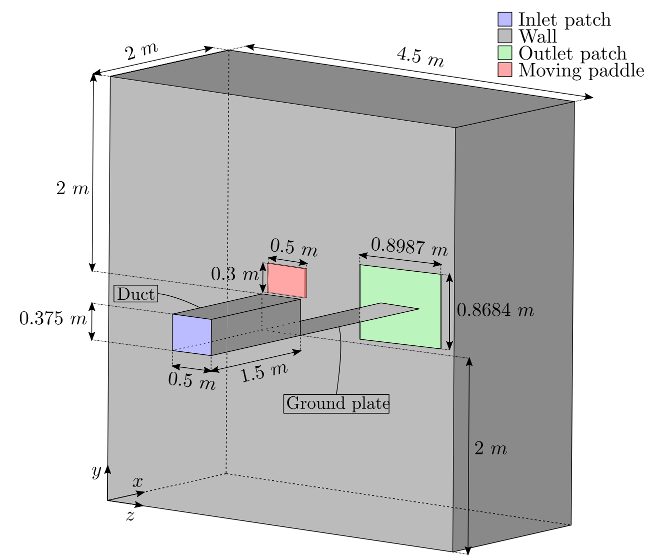

FIG. 5. Geometry of the test case and definition of the boundary conditions.

the boundary layers at the walls develop within the duct achieving a free-stream velocity $u_\infty = 5.14$ m/s at its outlet (identical to that of the experimental setup). No-slip and impermeability boundary conditions are applied on the walls of the duct, the far-field walls and the ground plate. A convective boundary condition is defined at the outlet patch (modeling the receiver of the wind tunnel) with a convective velocity of $u_{conv} = u_{inlet}^{steady}$.

The Eulerian grid is a block-structured Cartesian grid consisting of 36.6×10^6 control volumes. The total number of control volumes and their distribution is motivated by the following considerations. The geometric block-structure consisting of 10 blocks is split up into a parallel block-structure with 340 blocks. That allows a parallel execution on 340 cores with a load balancing efficiency of 100%. Grid refinement near relevant rigid walls (i.e., duct walls and ground plate) is essential to capture the significant viscous effects leading to the formation of thin boundary layers. The maximum first cell size positioning the first node (i.e., its cell center) within the viscous sublayer (i.e., $y^+ < 5$) is therefore sought. The hydraulic diameter of the rectangular duct (i.e., $D_h = 4wh/2(w+h) = 0.4286$) is used as a characteristic length to calculate the Reynolds number $\mathrm{Re} = \rho D_h u_\infty/\mu = 147,701$. The Darcy friction factor found by Moody[34] is

$$f = 0.0055\left[1 + \left(2 \times 10^{-4}\,\frac{k}{D_h} + \frac{10^6}{\mathrm{Re}}\right)^{\frac{1}{3}}\right], \tag{48}$$

where k is the pipe's effective roughness height. Assuming a smooth pipe (i.e., $k = 0$), the skin friction coefficient is evaluated by $c_f = f/4 = 3.97 \times 10^{-3}$. Hence, to resolve the near-wall region accurately, one could approximate the maximum height of the first grid cell off the wall (Δy) resulting in $y_{cc}^+ = 2$ at the cell center by $\Delta y/D_h = (4/\mathrm{Re}) \cdot \sqrt{2/c_f} \approx 6 \times 10^{-4}$ (i.e., $\Delta y \approx 2.6 \times 10^{-4}$ m). In order to reduce the computational costs, the grid is mildly stretched in the off wall directions with an expansion factor of 1.04. The same stretching factor is also applied in the streamwise direction. Starting with the finest grid at the outlet of the nozzle, where the paddle is located, the grid is mildly coarsened in the upstream and downstream directions. Based on the free-stream velocity, the stability of the explicit time integration scheme is ensured by choosing a time step size of $\Delta t = 2 \times 10^{-5}$ s leading to a Courant–Friedrichs–Lewy number less than 0.4.

A. Distribution of Lagrangian points describing the paddle

The geometry of the paddle is simplified by a parallelepiped of right angles with $L_2 = 0.3$ m and $L_3 = 0.5$ m. This simplification is assumed to have no effect on the results as in both cases (i.e., experiment and simulation) a rectangular cross-section will penetrate the flow exiting the nozzle. The moving paddle of thickness $L_1 = 3 \times 10^{-3}$ m is placed 0.015 m away from the outlet of the nozzle.

Two distributions of the Lagrangian markers used for the description of the paddle are investigated, namely, a uniform distribution and a one-dimensional non-uniform distribution described below. The uniformly distributed set of Lagrangian markers considered is shown in Fig. 6. The spacing between the markers is defined (in each coordinate direction) based on the minimum local Eulerian grid spacing (i.e., $\Delta x_{i,min}$ for $i = 1, 2$, and 3) that the paddle will pass by during its closing and opening stroke. This is to avoid any potential fluid penetration through the surface of the paddle arising from inadequate Eulerian

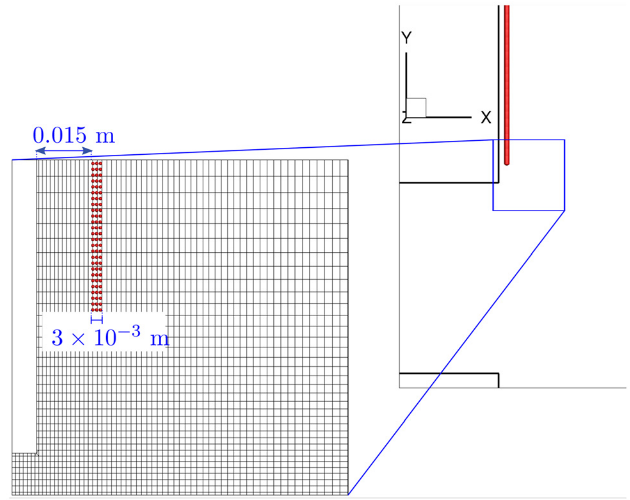

FIG. 6. Zoom of the nozzle outlet with the Eulerian grid and the uniformly distributed Lagrangian markers.

cells coverage by the Lagrangian markers window function. Thus, the Lagrangian grid spacings are defined based on the following two steps. The minimum local Eulerian grid spacing in each coordinate direction (here, it is the first cell size at a no-slip wall for y and z coordinates) is determined and used to evaluate the number of Lagrangian markers in each respective direction

$$N_i = \frac{L_i - \Delta x_{i,min}}{\Delta x_{i,min}} + 1. \tag{49}$$

The outcome of Eq. (49) (N_i) can be a decimal number. Since the number of Lagrangian markers can only be a natural number, Lagrangian grid spacings are therefore defined by rounding N_i up to the nearest integer as

$$\Delta X_i = \frac{L_i}{\lceil N_i \rceil}. \tag{50}$$

Based on the Eulerian grid employed, the number of Lagrangian markers in each direction is $\lceil N_1 \rceil = 3$, $\lceil N_2 \rceil = 1154$, and $\lceil N_3 \rceil = 1924$ (i.e., $N_L = \lceil N_1 \rceil \lceil N_2 \rceil \lceil N_3 \rceil = 6\,660\,888$). The corresponding Lagrangian grid spacings are $\Delta X = 1 \times 10^{-3}$ m and $\Delta Y = \Delta Z = 2.59 \times 10^{-4}$ m setting the volume associated with each Lagrangian force point to $\Delta V = \Delta X \Delta Y \Delta Z = 6.75 \times 10^{-11}\,\mathrm{m}^3$.

The simulation is seen to undergo a remarkable slowdown (8 times slower) due to the abundance of Lagrangian markers resulting from the uniform spatial distribution. This is primarily a consequence of the uneven distribution of Lagrangian markers among the parallel processors. Lagrangian markers are predominantly shared by a maximum of 12 out of the total 340 processors throughout the simulation. For each processor containing Lagrangian markers, an additional computational load arises from the interpolation, spreading, and tracking processes. Consequently, the time taken to perform one time step on the heavily burdened processors is significantly increased leading to an adverse affect on the overall performance.

Therefore, an alternative given by the one-dimensional non-uniform distribution is examined. In this enhanced variant, the distribution of the Lagrangian markers is left identical to the uniform distribution along the x and y axes. However, along the z axis, the distribution is defined in such a way that for each cell center a Lagrangian marker is assigned. In other words, Lagrangian markers are set to follow the grid stretching employed along the z axis. The reason for this choice lies in the fact that, during the paddle's opening and closing stroke, the distribution of Eulerian points along the z axis remains unchanged. This leads to a significantly reduced total number of Lagrangian markers of $N_L = 761\,640$ where $N_3 = 220$ and thus decreased by a factor of about 9. It is worth mentioning that with this approach the volume associated with the Lagrangian marker varies along the z axis which has to be taken into account in the algorithm.

B. Definition of the paddle's velocity

Wood, Breuer, and Neumann[1] investigated five different paddle motion patterns and analyzed their effects on the generated gusts. Each pattern is characterized by its own settings of the paddle's acceleration, velocity, and displacement during the downward and upward stroke. The main gust pattern used in their work (also denoted *Type* 1 pattern) is considered in this study as it imitates the standard 1-cosine symmetric gust shape defined in the IEC-Standard[23] as the Extreme Coherent Gust (ECG).

A smooth (differentiable) analytical function is fitted to the vertical velocity curve defined by the experiment as shown in Fig. 7. The fitted velocity function found reads

$$V_d(t) = \begin{cases} -A_1\left(3\phi_1^2 - 2\phi_1^3\right), & \text{if } t_{s,1} = 0\,\text{s} \le t < t_{e,1} = 0.07\,\text{s}, \\ -A_1, & \text{if } t_{e,1} \le t < t_{s,2} = 0.16\,\text{s}, \\ A_2\left(3\phi_2^2 - 2\phi_2^3\right) - A_1, & \text{if } t_{s,2} \le t < t_{e,2} = 0.33\,\text{s}, \\ A_2 - A_1, & \text{if } t_{e,2} \le t < t_{s,3} = 0.438\,\text{s}, \\ (A_2 - A_1) & \\ -(A_2 - A_1)\left(3\phi_3^2 - 2\phi_3^3\right), & \text{if } t_{s,3} \le t < t_{e,3} = 0.517\,\text{s}, \\ 0, & \text{otherwise}, \end{cases} \tag{51}$$

where $\phi_i = (t - t_{mid,i})/t_{w,i}$, $t_{mid,i} = (t_{e,i} + t_{s,i})/2$, $t_{w,i} = t_{e,i} - t_{s,i}$, $A_1 = 1.05$, and $A_2 = 2$. Like in the experiment, the offset displacement $\Delta y_{os} = 0.045\,\text{m}$ is the distance that the paddle needs to travel (when it is initially at its idle position) in order to start blocking the nozzle's outlet. This hinders the unwanted initial interaction between the paddle and the undisturbed free-stream flow and allows for the gradual buildup of the paddle's velocity preceding the interaction. The bell-shaped displacement pattern is then prescribed letting the paddle block a maximum of $\Delta y_{max} = 0.1437\,\text{m}$ of the nozzle's outlet [i.e., a blocking ratio (BR) of 0.383] and have a total interaction time of $\Delta t_{gust} = 0.352\,\text{s}$ (i.e., the time span between the two red circles in Fig. 7). The paddle is eventually brought back to rest at its idle position. Note that the present values of Δy_{max} and Δt_{gust} slightly deviate from those given in Wood, Breuer, and Neumann.[1] The reason is that the latter corresponds to the prescribed values of the tooth belt axis in the experimental setup, whereas the present values better describe the real measured motion pattern. It is worth mentioning that in the simulation it is sufficient to prescribe the no-slip vertical velocity of the paddle as its displacement is a derived value found by Eqs. (44)–(46).

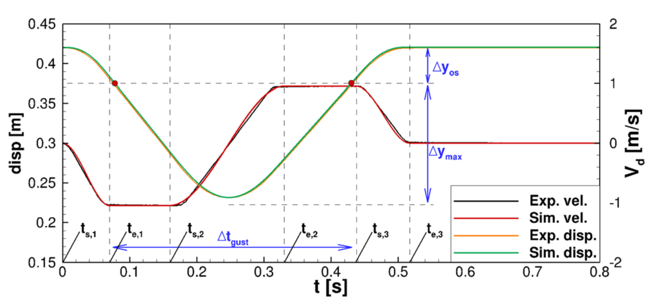

FIG. 7. Kinematic characteristics of the fitted *Type* 1 paddle movement pattern.

C. Definition of the inlet velocity variation

In Wood, Breuer, and Neumann,[1] an undershooting of the streamwise velocity below the free-stream velocity was observed at the nozzle's outlet during and after the paddle encounter. The authors explained this observation by conducting an additional closing stroke test (i.e., a sudden downward movement of the paddle without a subsequent upward movement). This undershooting phenomenon is attributed to the paddle acting as a bluff body blocking the fluid flow and thus causing high pressure losses due to the paddle in the fluid stream. Since the blower is not operated in a mode that allows to compensate these higher pressure losses appearing in the wind tunnel, less air is blown through the wind tunnel causing an undershoot below the free-stream velocity. Note that even a fully controlled operation of the blower might not be able to avoid this phenomenon owing to its long response time. Further opening stroke tests (i.e., a sudden upward movement of the paddle after staying in the fluid flow over a long time period) have clearly shown that the recovery time until the free-stream velocity is reached again, is much longer than Δt_{gust}. In order to account for this inlet velocity drop, Constant Temperature Anemometry (CTA) measurements recorded inside the nozzle during the gust generation process[35] are used to define a time-dependent inlet boundary condition as shown in Fig. 8. The inlet velocity function defined reads

$$u_{inlet}(t) = \begin{cases} u_{inlet}^{steady}, & \text{if } 0\,\text{s} \le t < t_{s,1}^{in} = 0.076\,\text{s}, \\ u_{inlet}^{steady} - A_3\left(3\phi_1^2 - 2\phi_1^3\right), & \text{if } t_{s,1}^{in} \le t < t_{e,1}^{in} = t_{s,2}^{in} = 0.3\,\text{s}, \\ (u_{inlet}^{steady} - A_3) + A_3\left(3\phi_2^2 - 2\phi_2^3\right), & \text{if } t_{s,2}^{in} \le t < t_{e,2}^{in} = 1.588\,\text{s}, \\ u_{inlet}^{steady}, & \text{otherwise}, \end{cases} \tag{52}$$

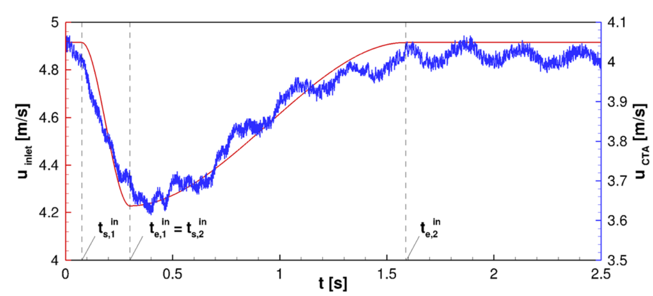

FIG. 8. Time-dependent inlet boundary condition and CTA measurements in the nozzle.[35]

where ϕ_i is defined in a similar manner as in Eq. (51) and A_3 is set to 0.686. Note that a direct comparison of the amplitudes between the prescribed inlet velocity function and the CTA measurements is not meaningful, since the latter were carried out somewhere in the converging part of the wind tunnel nozzle.

VI. RESULTS

The results presented are mainly based on the simulation with the one-dimensional non-uniform distribution of Lagrangian markers. This is due to the fact that both alternatives deliver nearly the same results. Therefore, in order to save computational resources, the second alternative of Lagrangian markers distribution is primarily employed. A comparison of the results obtained by both distributions is carried out in the Appendix.

A. Flow field induced by the wind gust generator

In the following, results showing the evolution of the flow during the gust generation process by means of the moving paddle are provided. Figure 9 points out the time instants at which the fields in Figs. 10 and 11 are taken. These visualizations depict the streamwise and vertical velocity components as well as the pressure and the vorticity component in z-direction for a x-y cross-section in the center of the duct. At instant 1, the paddle is at its idle position, and the fields represent the initial conditions used for the simulations where the flow is initially allowed to fully develop for 10 s. Two flow phenomena are clearly visible. On the one hand, boundary layers develop along the top and bottom wall of the duct. For the latter, the development of the boundary layer continues along the ground plate. On the other hand, a free shear layer is formed in the region resulting from the horizontal continuation of the upper duct wall. At instant 2, the flow starts to deviate from its original stream as the paddle blocks 15.8% of the nozzle's outlet. This causes the streamwise velocity to accelerate and the vertical velocity to build up negative values below the paddle. The positive vertical velocity at the small gap between the nozzle's outlet and the paddle indicates fluid escaping from that region as well. While a pressure rise is observed in front of the paddle, a strong vortical structure with a pressure minimum in its center starts to form at the backside of the paddle as also visible in the vorticity distribution in Fig. 11(b). That is due to the fluid separation taking place at its bottom edge. At instant 3, the paddle continues its downstroke reaching a

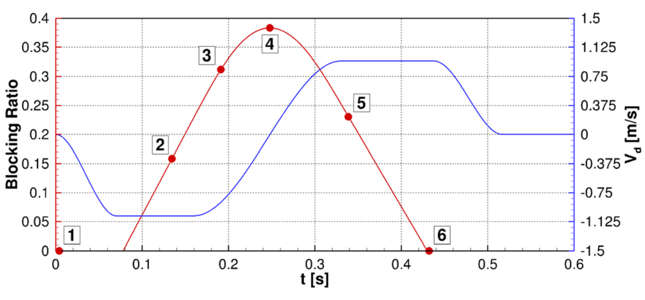

FIG. 9. Nozzle's blocking ratio (red line) annotated with visualization time instants and paddle's vertical velocity (blue line) during the downward and upward strokes. Instant 1: paddle at idle position, instant 2: 15.8% blocking ratio, instant 3: 31.2% blocking ratio, instant 4: 38.3% blocking ratio (maximum), instant 5: 22.0% blocking ratio, and instant 6: paddle just left nozzle's outlet.

blocking ratio of 31.2%. A higher streamwise velocity extending to the ground plate and higher pressure values extending upstream of the duct are recorded as the flow in the outlet is further contracted. Note that this pressure rise and the associated decrease in the streamwise velocity in front of the paddle is the reason for defining a transient inlet velocity function provided in Sec. V C. The size of the strong vortex originating from the bottom edge of the paddle increases, and the vortical structure is convected downstream. A new shear layer develops behind the paddle's edge which follows its motion. At instant 4, the paddle arrives at its maximum blocking ratio of 38.3%. Obviously, in the remaining outlet region above the ground plate, the streamwise velocity reaches high values which characterize the resulting strong horizontal gust. This describes the main effect to be achieved by the paddle motion. A side effect is that the pushed fluid stream also possesses a downward velocity component directed toward the ground plate. At this instant in time, the area unaffected by the shear layer reaches its minimum. The new shear layer developing at the paddle's bottom edge breaks up into a series of small vortices while the large vortex is further convected downstream. At instant 5, the paddle starts traveling back to its idle position (i.e., upward stroke) where its blocking ratio reduces to 22.0%. At this stage, the large vortical structure hits the ground plate and the strength of the generated gust already decreases again resulting in highly transient velocity fields. The approach of the vortex at the ground plate has certain consequences for the remaining part of the flow field. When the vortical structure reaches the plate, it lifts up the boundary layer on the ground plate. Thus, a small region of low streamwise velocity is observed close to the bottom wall, while at the same time, the vertical velocity is positive in this area pointing away from the wall. At instant 6, the paddle leaves the nozzle's outlet and the process of flow recovery to the initial state starts.

B. Spanwise characteristics of the generated gust

In the following, the spanwise characteristics of the gust are discussed. Given the results in Figs. 10 and 11 and the experimental analysis of Wood, Breuer, and Neumann,[1] the schematic sketch shown in Fig. 12 illustrates the regions formed during the gust generation process using the paddle. The zones are denoted the free shear layer region and the undisturbed gust region. The latter zone indicates the region where a stable gust forms with a good experimental reproducibility. The size of these regions strongly depends on the maximum displacement of the paddle where larger displacements lead to a smaller undisturbed gust region. For feasibility purposes, the origin of the coordinate system chosen for the Laser-Doppler Anemometer (LDA) measurements in Wood, Breuer, and Neumann[1] was shifted by an offset $\Delta x_{\mathrm{LDA}} = 0.06\,\mathrm{m}$ away from the nozzle's outlet. The shifted and normalized coordinate system (normalized by the width of the nozzle's outlet) shall now be employed to describe different positions in the following. Figures 13 and 14 depict the evolution of velocity components at the x-planes $x/w = 0$ and $x/w = 0.2$, respectively. The latter cross-section is specifically chosen, since it corresponds to the beginning of the region typically used to place an FSI model in the test section. Although the edges of the paddle are illustrated on the same plane, it is important to note that they are positioned behind the plane. They are projected both to enhance visualization and to provide a reference for tracking the position of the paddle.

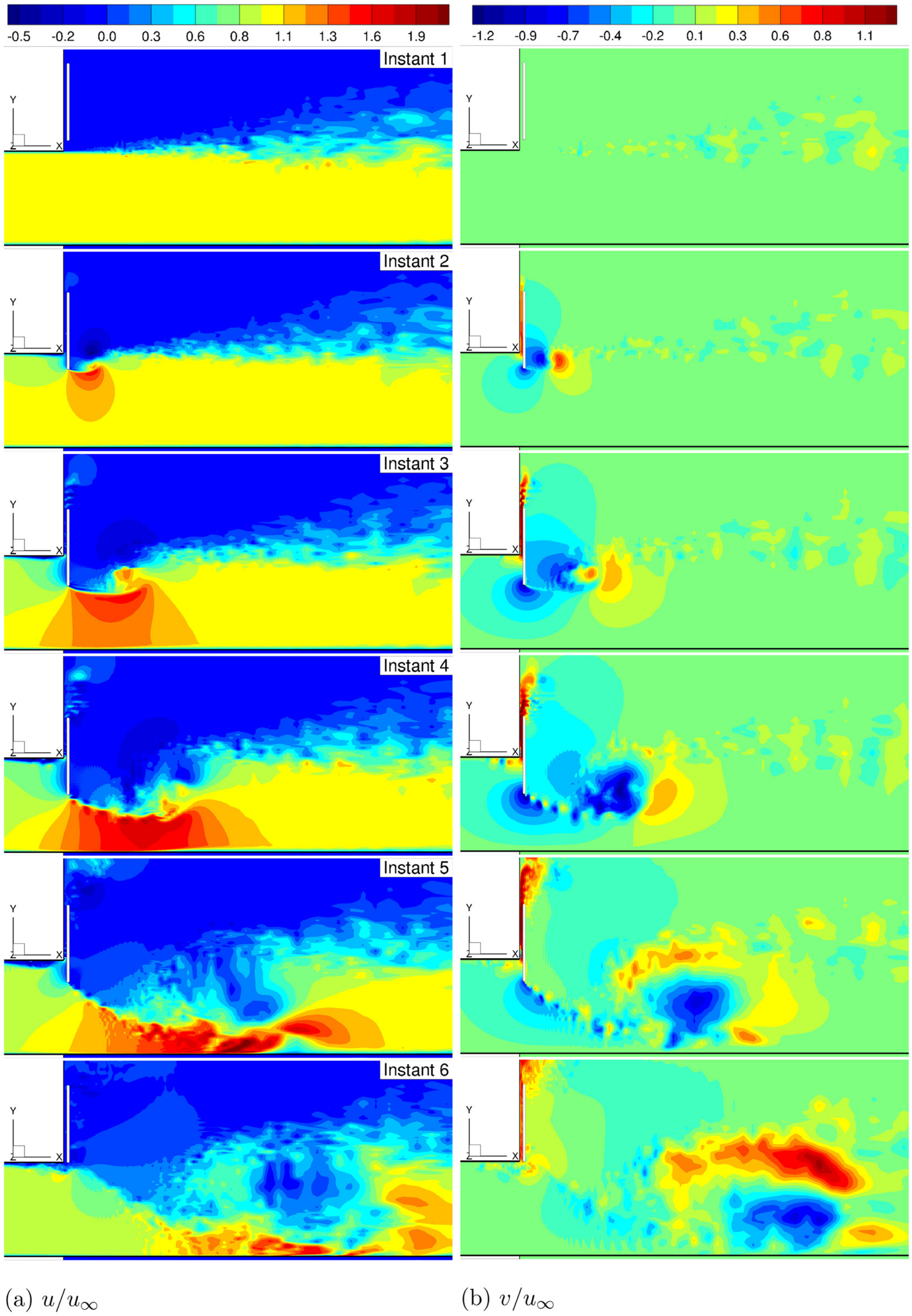

FIG. 10. Snapshots of the (a) streamwise velocity and the (b) vertical velocity during the paddle's downward and upward strokes. Instants correspond to those depicted in Fig. 9.

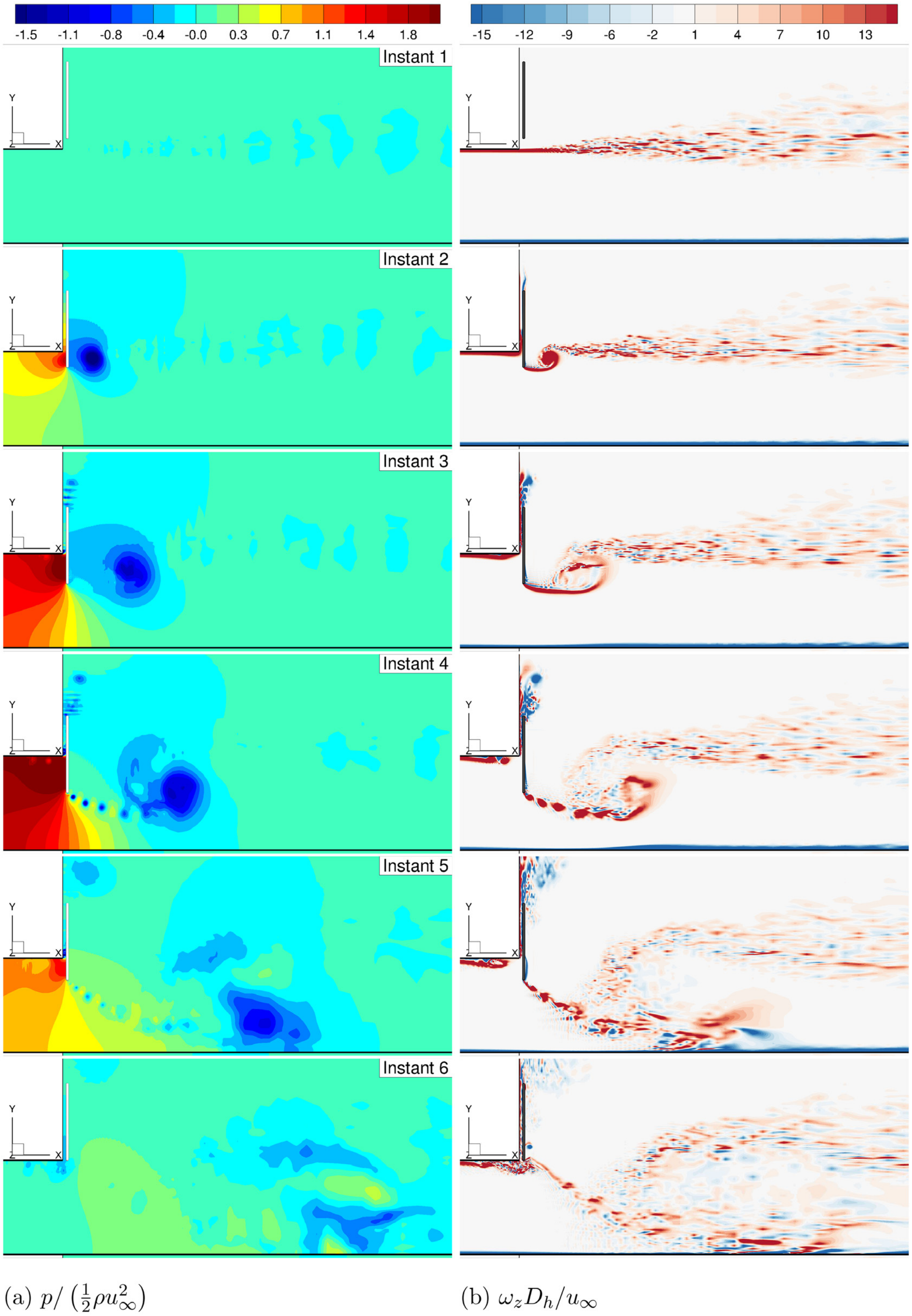

FIG. 11. Snapshots of the (a) pressure and the (b) z-vorticity ω_z during the paddle's downward and upward strokes. Instants correspond to those depicted in Fig. 9.

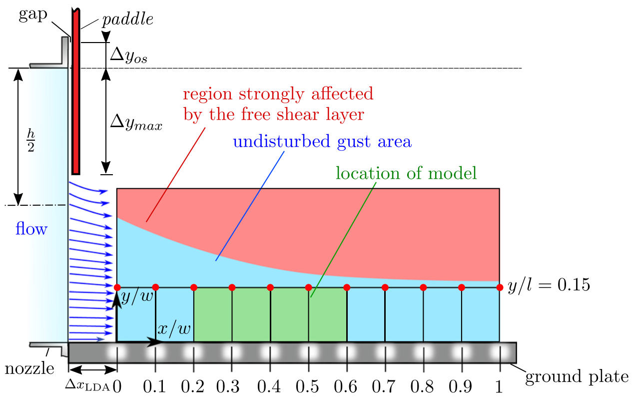

FIG. 12. Schematic sketch of flow regions and the usable space for gust investigations (adjusted with permission from Wood *et al.*, J. Wind Eng. Ind. Aerodyn. **230**, 105170 (2022). Copyright 2022 Author(s), licensed under a Creative Commons Attribution (CC BY) license.

First, the spanwise characteristics of the gust at the x-plane $x/w = 0$ are discussed (see Fig. 13). At instant 1, the flow is predominantly influenced by the free-stream velocity, which experiences a rapid decline to zero in the proximity of the duct's walls. Throughout this region, both the y- and z-components of the velocity are zero as expected since presently no inflow turbulence is taken into account. Advancing to instant 2, as the paddle begins its penetration of the nozzle's outlet, a symmetric velocity pattern emerges for all three components. The streamwise velocity exhibits a nearly uniform increase along the z axis beneath the paddle. However, closer to the ground plate, this uniformity is disturbed, revealing slightly higher streamwise velocities at the free ends (i.e., the left and right edges). This behavior can be attributed to the fluid's tendency to follow the path of least resistance. Simultaneously, a negative vertical velocity emerges due to the downward movement of the paddle and the formation of a strong vortical structure on the backside of the paddle. Except at the free ends the contour lines of the vertical velocity are approximately parallel to the ground plate. Additionally, a spanwise velocity component initiates directing the fluid toward the left and right edges of the ground plate. A careful examination of the y- and z-velocity fields in the lower left and right corners of the paddle reveals the development of clockwise and counterclockwise rotating vortices, respectively. Note that an additional simulation with a paddle elongated in both positive and negative z-directions has shown that the relevant flow field in the measurement region of the wind tunnel is only marginally influenced by this extension. At instants 3 and 4, all velocity components persistently increase in magnitude within the region unobstructed by the paddle. A highly transient flow characterizes the paddle's left and right edges due to the fluid separation taking place. To provide a visual impression of the generated gust, Fig. 15 depicts an isometric view based on the isosurface of the streamwise velocity ($u/u_\infty = 1.38$). At instant 5, as the paddle is returning to its idle position, an overall reduction in the streamwise velocity is observed. However, this time, the maximum streamwise velocity is not positioned directly beneath the paddle but close to the ground plate. This shift (w.r.t. instant 2) is attributed to the strongly decelerated flow field in front of the paddle visible in Fig. 10(a) (instants 3 to 5) which is released when the paddle leaves the nozzle. While the unobstructed region below the paddle experiences a decrease in the magnitude of the negative vertical velocity, the region above the paddle reaches positive velocities, following the shear layer generated by the paddle's upward motion. Finally, at instant 6, as the paddle is completely withdrawn from the nozzle's outlet, all velocity fields undergo a gradual return to their initial states.

An analysis of the flow field further downstream at the x-plane $x/w = 0.2$ (see Fig. 14) reveals a noteworthy finding regarding the spanwise characteristics of the generated gust. It can be observed that the flow field possesses an increased level of homogeneity in z-direction, particularly in its streamwise component. Another observation is the symmetric distribution of the z-component of the velocity at the free ends driving the flow out of the x-y plane (i.e., expanding the flow in the spanwise direction). Compared to the cross-section at $x/w = 0$ (Fig. 13), the level increases further downstream at $x/w = 0.2$ (Fig. 14).

Concluding the observation described above, the following can be stated. Excluding from both spanwise edges about 20% of the total width ($w = 0.5$ m) and despite the minor effect of the z-velocity component in that region, the flow field generated by the paddle can be considered as nearly homogeneous in the spanwise direction. That is in full agreement with the experimental outcome of Wood, Breuer, and Neumann[1] who detected nearly constant streamwise velocity component of the generated gust for this spanwise range. Nevertheless, two important issues have to be mentioned here when confronting the predictions with the experimental data. First, the LDA measurements were restricted to two velocity components, and thus, the spanwise velocity was not considered at all. Second, the main measurements were solely carried out for the geometric symmetry plane ($z = w/2$) where also in the predictions vanishing spanwise velocity components are found. Thus, the simulations have provided new insight into the flow field generated by the paddle which were not obvious from the measurements. For the planned FSI experiments and the corresponding simulations, these characteristic features of the gust (homogeneity in spanwise direction in the kernel of the gust and outward pointing spanwise velocity) have to be taken into account.

C. Comparison of numerical and experimental results

A validation of the proposed numerical method is carried out by a direct comparison with the experimental results of Wood, Breuer, and Neumann.[1] The comparison is performed in the symmetry plane at seven streamwise positions in the range $0 \leq x/w \leq 0.6$ and a height of $y/w = 0.15$ (see Fig. 12). This covers the region in which a wind tunnel model is typically placed in. Due to the presence of a shear layer at the top surface of the jet exiting the nozzle and the high Reynolds number considered, small vortical structures are irregularly formed and convected downstream as shown at instant 1 in Fig. 11(b). Consequently, the flow generated by the paddle's motion is dependent on the state of the flow at which the paddle is entering the nozzle's outlet. Henceforth, ensemble-averaged numerical results based on 25 initial condition states spanning from 10 to 22 s of the initial simulation without the paddle are considered. An interval of 0.5 s is chosen to separate the different initial conditions. The choice is based on a detailed examination of the flow variables at the shear layer, which revealed that for the chosen time interval the flow states exhibit statistical independence. The ensemble-averaged LDA measurements of the streamwise velocity and its numerical counterpart are depicted in Fig. 16.

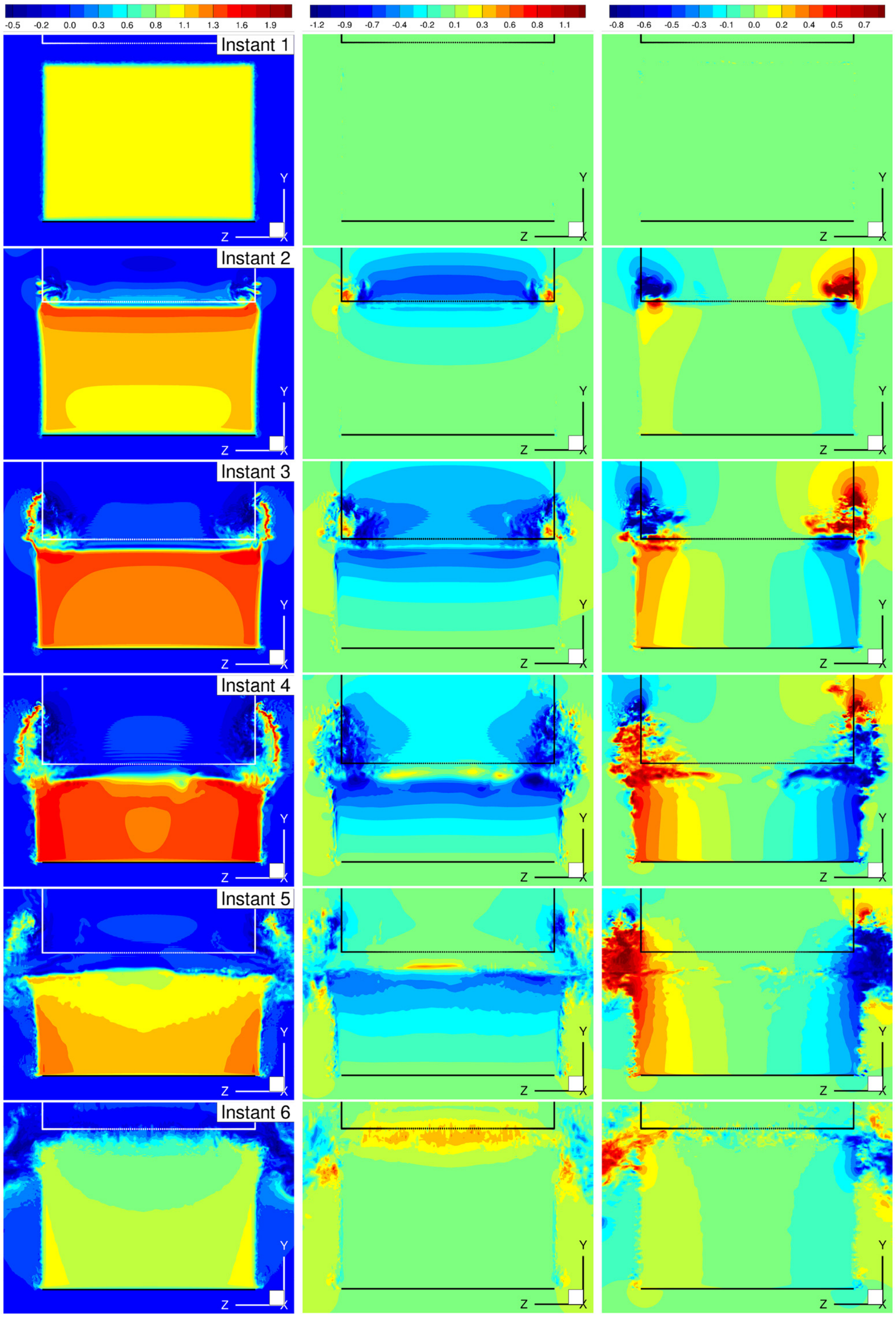

(a) u/u_∞ (b) v/u_∞ (c) w/u_∞

FIG. 13. Snapshots of the (a) streamwise velocity, the (b) vertical velocity, and the (c) spanwise velocity fields at the x-plane $x/w = 0$ during the paddle's downward and upward strokes. Instants correspond to those depicted in Fig. 9.

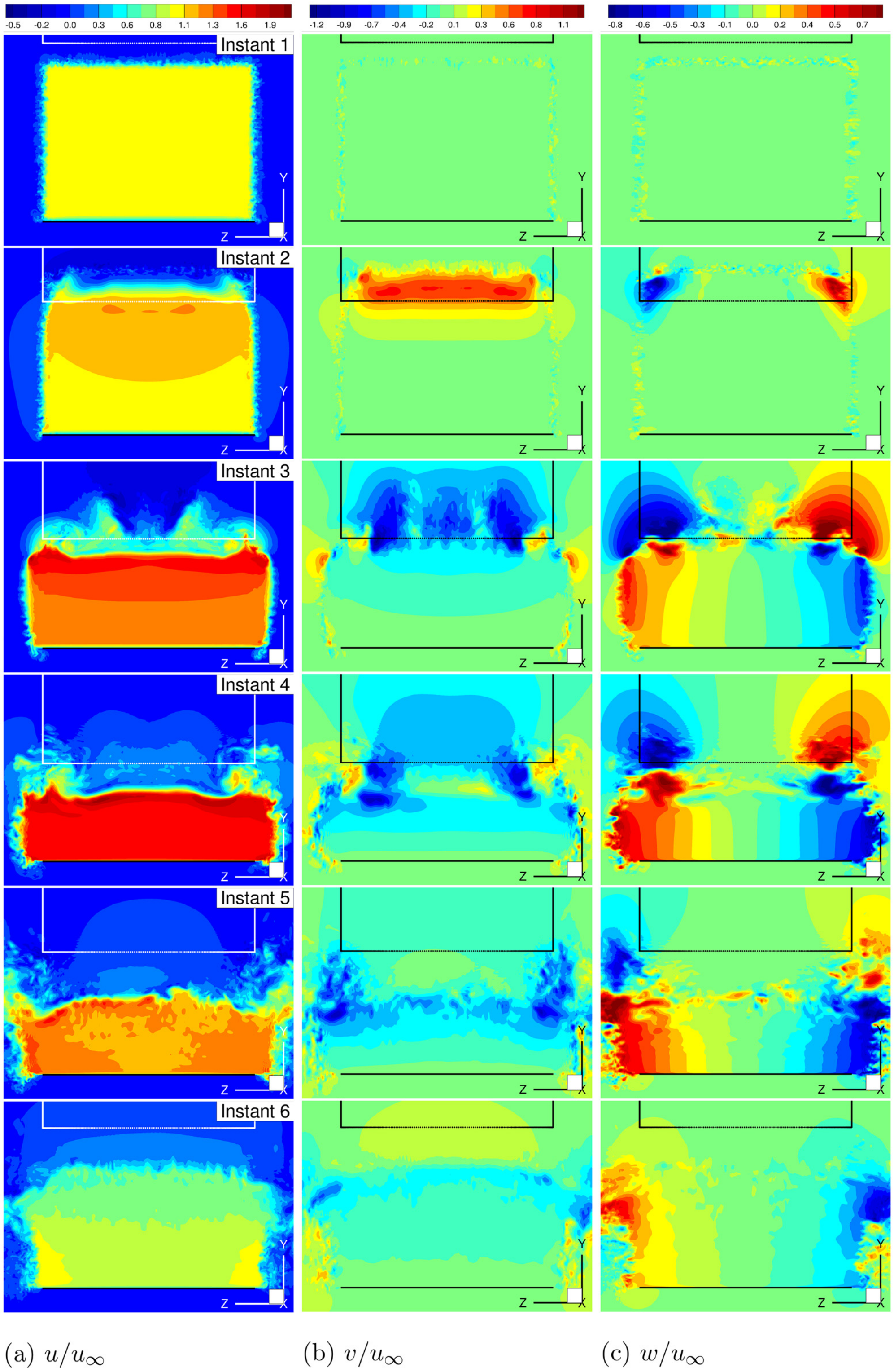

FIG. 14. Snapshots of the (a) streamwise velocity, the (b) vertical velocity, and the (c) spanwise velocity fields at the *x*-plane $x/w = 0.2$ during the paddle's downward and upward strokes. Instants correspond to those depicted in Fig. 9.

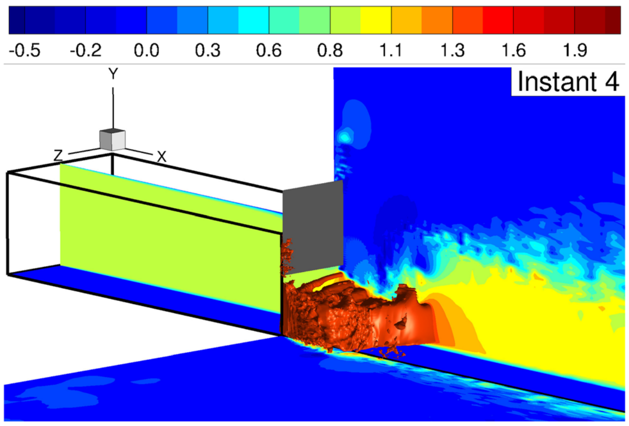

FIG. 15. An isometric view of the generated gust. All planes depict the streamwise velocity, and the gust structure is highlighted at instant 4 with the iso-surface $u/u_\infty = 1.38$.

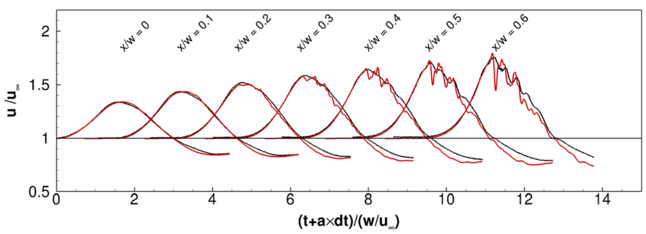

FIG. 16. Comparison between the ensemble-averaged experimental streamwise velocity u/u_∞ (black) reprinted with permission from Wood *et al.*, J. Wind Eng. Ind. Aerodyn. **230**, 105170 (2022). Copyright 2022 Author(s), licensed under a Creative Commons Attribution (CC BY) license and its numerical counterpart (red) of the gust generated by the paddle at the first seven points in Fig. 12.

The data are initially time-shifted to align the instant $t^* = t/(w/u_\infty) = 0$ with the beginning of the paddle blocking the outlet of the nozzle. To enhance the visibility of the data for the different streamwise locations, the time histories of the flow variables are shifted by adding the product of a freely chosen time increment of $\Delta t_{inc} = 0.15$ s and a spacing factor $a \in (0, \ldots, 6)$.

Focusing on the time history at a single point (e.g., $x/w = 0$), the streamwise velocity possesses a bell-shaped pattern that is consistent with the displacement curve of the paddle (see Fig. 7). As the paddle initially blocks the nozzle's outlet, it effectively reduces the available outlet area. According to the principle of mass conservation, the flow beneath the paddle is forced to accelerate to counterbalance this reduction in the outlet area. The flow acceleration continues until the maximum displacement of the paddle is reached. Subsequently, as the paddle starts traveling back to its idle position, the streamwise velocity decelerates (due to the increase in the outlet area) and even drops below the free-stream velocity (due to the transient inlet velocity defined in Sec. V C). Eventually, the free-stream velocity is recovered.

It can be observed that the numerical results exhibit a remarkable coincidence with the experimental results, affirming the fidelity of the numerical method applied. Two key observations confirm this agreement. In the range $0 \leq x/w \leq 0.3$, the streamwise velocity curves closely mirror those observed in the experimental data. Moreover, both results consistently illustrate the prominent increase in the maximum streamwise velocity as one moves along the downstream direction. This increase will be elaborated upon when the time history of the pressure at these points is discussed. As one progresses toward positions within the range $x/w \geq 0.4$, an additional phenomenon occurs. The descending slope of the streamwise velocity begins to exhibit a more chaotic and turbulent character. Comparable oscillations are observed in the ensemble-averaged data of Wood, Breuer, and Neumann,[1] but those mainly initiated slightly further downstream at $x/w = 0.5$. Looking at the time histories of the instantaneous data

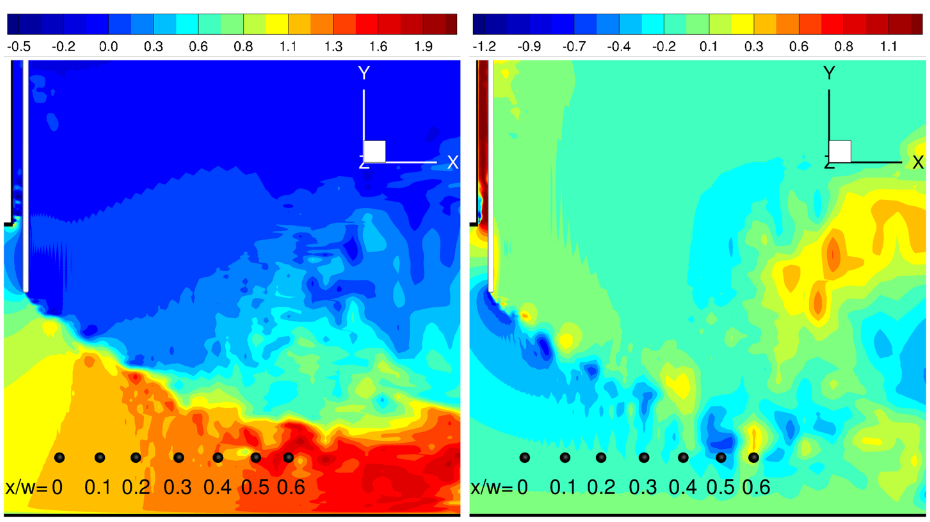

(a) u/u_∞. (b) v/u_∞.

FIG. 17. Snapshot of the (a) instantaneous streamwise velocity and the (b) instantaneous vertical velocity fields at instant 5. The first seven points in Fig. 12 are marked for reference.

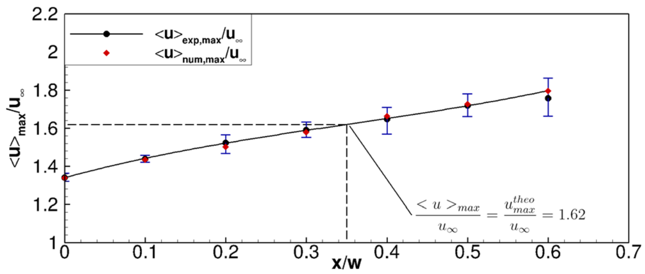

FIG. 18. Comparison between the maximum ensemble-averaged experimental streamwise velocity u/u_∞, including the velocity range (error bars) reprinted with permission from Wood *et al.*, J. Wind Eng. Ind. Aerodyn. **230**, 105170 (2022). Copyright 2022 Author(s), licensed under a Creative Commons Attribution (CC BY) license and its numerical counterpart at the first seven points in Fig. 12.

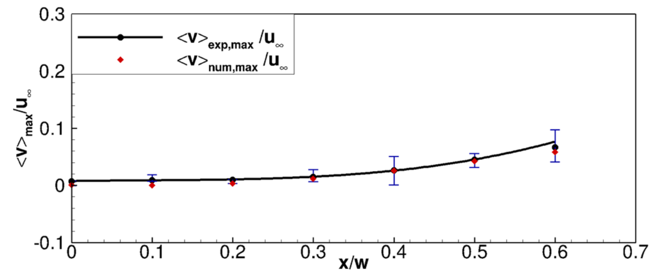

FIG. 20. Comparison between the maximum ensemble-averaged experimental vertical velocity v/u_∞ including the velocity range (error bars) reprinted with permission from Wood *et al.*, J. Wind Eng. Ind. Aerodyn. **230**, 105170 (2022). Copyright 2022 Author(s), licensed under a Creative Commons Attribution (CC BY) license and its numerical counterpart at the first seven points in Fig. 12.

of single events (not shown here for brevity), the amplitudes of the fluctuations are even significantly larger than for the ensemble-averaged data. That holds true for both the simulations and the measurements. These velocity fluctuations are attributed to the free shear layer and the vortices shed from the bottom edge of the paddle as shown in Fig. 17(a). Obviously, even 25 simulations are not sufficient to average these chaotic fluctuations out.

Figure 18 depicts the maximum ensemble-averaged experimental streamwise velocity (i.e., $\langle u\rangle_{\exp,max}/u_\infty$) and its numerical counterpart (i.e., $\langle u\rangle_{num,max}/u_\infty$) at the selected positions. Based on $\langle u\rangle_{\exp,max}/u_\infty$, Wood, Breuer, and Neumann[1] employed a third-order polynomial curve fitting (black line) to predict the maximum streamwise velocity at locations within the range $0 \le x/w \le 0.6$. At each measurement point and based on the 25 experimental realizations, error bars are employed to define a velocity range by marking the extremal experimental values. Obviously, the numerically predicted mean values $\langle u\rangle_{num,max}/u_\infty$ fit very well to the experimental counterparts for $x/w \le 0.5$. At the last point evaluated ($x/w = 0.6$), a slight deviation is visible, which can be attributed to the less realizations in the simulations. Nevertheless, the predicted value stays within the measured velocity range. Furthermore, two previously discussed characteristics can be highlighted. The first is concerned with the increase in the maximum streamwise velocity along the streamwise direction, evident by the positive slope of the curve. The second characteristic is related to the increased chaotic behavior within the region $x/w \ge 0.4$ as indicated by the expansion of the error bars. Furthermore,

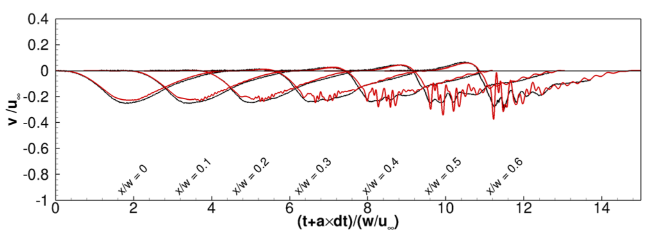

FIG. 19. Comparison between the ensemble-averaged experimental vertical velocity v/u_∞ (black) reprinted with permission from Wood *et al.*, J. Wind Eng. Ind. Aerodyn. **230**, 105170 (2022). Copyright 2022 Author(s), licensed under a Creative Commons Attribution (CC BY) license and its numerical counterpart (red) of the gust generated by the paddle at the first seven points in Fig. 12.

one can express the theoretical maximum streamwise velocity as a function of the maximum blocking ratio [here max(BR) = 0.383] by $u^{theo}_{max}/u_\infty = (1 - \max(\mathrm{BR}))^{-1} = 1.62$. According to the fitted curve, this value falls at $x/w = 0.35$ (i.e., within the region where a FSI model is commonly positioned). Note that these values are slightly different from the data in Wood, Breuer, and Neumann[1] (maximum theoretical velocity of 1.63 and its corresponding location at 0.36). The reason is that Wood, Breuer, and Neumann[1] used the prescribed paddle displacement for their calculation leading to a slightly different blocking ratio of $\mathrm{BR}_{\exp} = 0.387$. However, the recorded (real) displacement used in the prediction is slightly less.

An analogous agreement of the experimental and the numerical results is evident in the wall-normal velocity component (see Fig. 19). The vertical velocity mainly exhibits negative values, indicating that the flow is directed toward the ground plate. This behavior is consistent with the displacement curve of the paddle. During its downstroke, the paddle gradually guides the jet exiting the nozzle's outlet downward. However, during its upward stroke, it steadily reduces its steering effect on the flow, allowing the jet to return to its original trajectory. Beyond the range $x/w \ge 0.3$, increasing positive vertical velocities are initially observed. These are attributed to the strong counterclockwise rotating vortex forming at the bottom edge of the paddle during its downstroke [see instants 2 to 4 in Fig. 10(b)]. Similar to the velocity in the streamwise direction, a strong increase in the fluctuations becomes obvious in this region. This can be again attributed to the strong shear layer developing from the lower edge of the paddle as shown in Fig. 17(b). Even in the ensemble-averaged LDA data these fluctuations are still visible in Fig. 19.

Analogous to Fig. 18, Fig. 20 depicts the maximum values of the vertical velocity. It is important to mention that the maximum

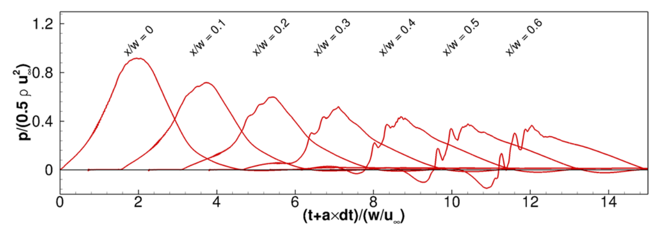

FIG. 21. Predicted ensemble-averaged pressure at the first seven points in Fig. 12.

velocities under consideration pertain solely to the initial surge phase, rather than encompassing the entire curve. The maximum wall-normal velocity (see Fig. 20) displays values near zero at points in the close proximity to the paddle (i.e., for $x/w \leq 0.2$). However, in the region $x/w \geq 0.3$, a steady increase along the streamwise direction is observed. Again, predictions and measurements are found to be in close agreement. Note that the minimum values are not depicted here for the following reason. Despite phase averaging both datasets still show very large fluctuations, so that a direct comparison makes no sense.

Employing numerical simulations facilitates the extension of the analysis to examine the time history of the pressure depicted in Fig. 21. It is important to emphasize that a direct comparison with the experimental data is unattainable due to the exclusive provision of velocity signals by the LDA measurements. A contrasting trend of the pressure curves is observed compared to the streamwise velocity signals, i.e., pressure peaks decrease in downstream direction. This behavior can be explained as follows. As clearly visible in Fig. 11(a), the blocking of the nozzle's outlet by the paddle leads to a strong increase in the pressure in the upstream region. Obviously, this effect decreases again as the distance from the nozzle increases [see pressure contour lines at the instants 2 to 5 in Fig. 11(a)]. This explains the inverse correlation between the pressure peaks and the distance of the points from the nozzle's outlet. Furthermore, this decrease in the pressure generates a negative pressure gradient that evokes the streamwise velocity to accelerate in the downstream direction. The pressure minima recorded in the region $x/w > 0.5$ are attributed to the large vortical structure originating from the bottom edge of the paddle during its downstroke [see instant 3 in Fig. 11(a)]. This vortical structure impacts the data evaluation points within this region before it gets convected downstream and pressure maxima emanating from the outlet are attained.

Finally, it should be mentioned that the IB method introduced in Sec. III does not lead to any numerically induced pressure oscillations. This is due to the compliance of the numerical method employed with the basic laws of physics. The external forces (represented by the hydrodynamic interactions) acting on a material point (i.e., a Lagrangian marker) are first evaluated based on Newton's second law. Then, these forces are transferred to the flow by smoothly distributing the Lagrangian forces to the neighboring Eulerian cells. This transfer is accomplished by the use of a regularized delta function that fulfills a set of conservation properties (including force and moment). Consequently, it ensures the satisfaction of Newton's third law of motion while keeping the incompressibility constraint intact.

Such smooth pressure curves are unattainable when less sophisticated approaches are used to simulate the paddle's motion. For example, the abrupt stepwise blocking of cells existing within the paddle's volume, achieved by the brutal prescription of all velocity components, leads to significant pressure oscillations as the paddle begins blocking the outlet. This issue emerges as the pressure solver struggles with the challenge of preserving the pressure–velocity coupling and adhering to the incompressibility constraint within the blocked cells.

D. Forces acting on the fluid by the moving paddle

Analyzing the force coefficients provides deeper insight into the underlying physics of the interaction between the flow and the paddle. This is facilitated by the fact that interpolation and spreading operators maintain the conservation of both force and moment [see Eqs. (20) and (21)]. Therefore, the total force can be readily calculated by summing the contributions from all Lagrangian points. Defining the reference area as the maximum area blocked by the paddle (i.e., $A_{ref} = w\,\Delta y_{max}$), the Lagrangian force coefficients read

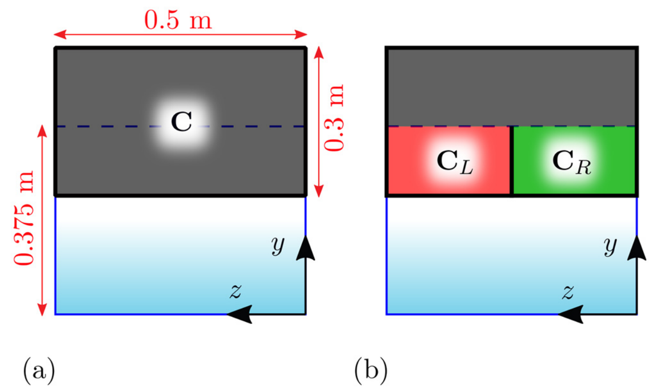

FIG. 22. Schematic sketch showing the different regions of Lagrangian markers considered in which the force coefficients are evaluated. (a) The entire paddle and (b) the direct interaction region split up into left and right halves.

$$\mathbf{C} = \frac{\sum_{l=1}^{N_L} \mathbf{F}(\mathbf{X}_l)\,\Delta V_l}{\frac{1}{2}\,\rho\,u_\infty^2\,A_{ref}}. \tag{53}$$

Identical force coefficients must be obtained if the force is evaluated with respect to the Eulerian frame of reference (i.e., $\mathbf{C} = \mathbf{c}$). This can be numerically verified by replacing the numerator of Eq. (53) with the left-hand side of Eq. (20). When analyzing the force coefficients, it is crucial to consider how the Lagrangian forces are defined. As per Eq. (12), the sign (hence, the direction) of a Lagrangian force is determined by the difference between the prescribed velocity of the immersed boundary (i.e., $\mathbf{U}_d(t) = [0, V_d(t), 0]$) and the interpolated fluid velocity in its vicinity [i.e., $\mathcal{I}(\mathbf{u}^*)$]. Figure 23 depicts the temporal evolution of the ensemble-averaged Lagrangian force coefficients and their Eulerian counterpart for the entire paddle [see Fig. 22(a)]. It is important to note that these coefficients pertain to the force exerted by the paddle on the flow (in contrast to the classical perspective). For all force coefficients, both curves (i.e., Lagrangian and Eulerian) align perfectly. This verifies the rigorous conservation of the force in the numerical method employed. Note that the conservation of the moments was also checked (not depicted here) and found to be fully satisfied.

To facilitate a better understanding of the results, the temporal evolution of the ensemble-averaged Lagrangian force coefficients focusing exclusively on the Lagrangian markers located in the region of the direct flow-paddle interaction (i.e., excluding those above the nozzle's outlet) is depicted in Fig. 24. These Lagrangian markers are further split up into the left and right half of the paddle depending on their spanwise location [see Fig. 22(b)].

The x-component of the force coefficient on the entire paddle [see Fig. 23(a)] has initially a zero value until the paddle begins blocking the nozzle's outlet. Then, this drops below zero indicating the

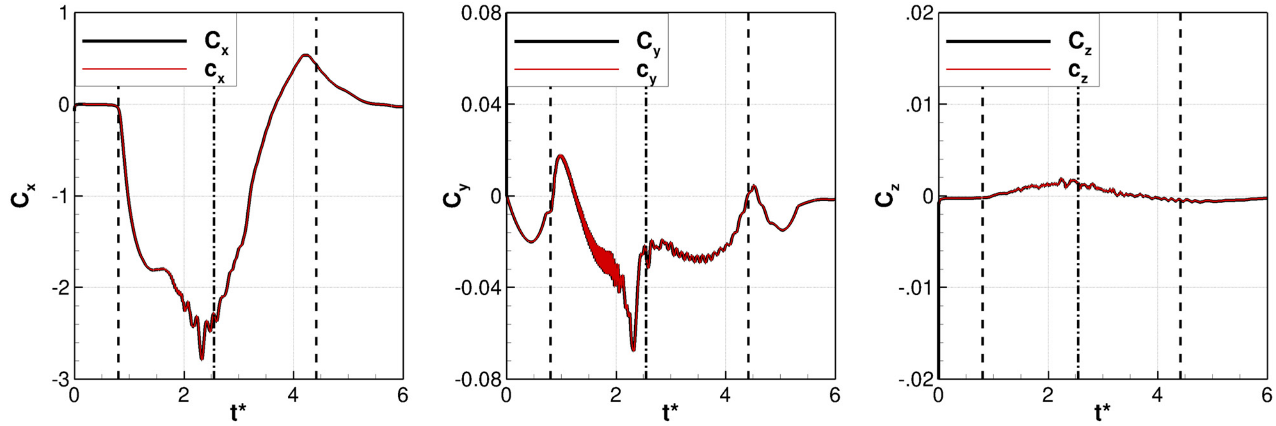

(a) x-force coefficient. (b) y-force coefficient. (c) z-force coefficient.

FIG. 23. Temporal evolution of the ensemble-averaged Lagrangian force coefficients evaluated over all Lagrangian markers [i.e., Fig. 22(a)] and their Eulerian counterpart. Dashed lines mark Δt_{gust}, the dashed-dotted line marks the maximum blocking.

paddle's resistance to the flow in the streamwise direction. This counteracting force continues to increase until it records its maximum magnitude slightly before the maximum blocked area is reached. As the paddle starts returning back to its idle position, the opposing force starts to steadily decrease and even exhibit positive values as the paddle completely leaves the nozzle's outlet. This is attributed to the negative streamwise velocity in the vicinity of the paddle during this phase [e.g., see instant 6 in Fig. 10(a)] and the associated low pressure [see instant 6 in Fig. 11(a)]. Furthermore, by considering Fig. 24(a) which depicts the force coefficient related to the blocked region only, it becomes evident that the zone above the nozzle's outlet is the source for the temporal asymmetry and the fluctuations in the x-component of the force coefficient. Due to the inherent geometric symmetry of the problem, the equal x-forces exerted by the left and right halves of the paddle within the direct interaction region indicate the symmetry of the x-velocity component.

The y-component of the force coefficient on the entire paddle [see Fig. 23(b)] exhibits a more complex behavior compared to the x-component. Note, however, that the values of the force in y-direction are about two orders of magnitude smaller than for the x-direction. It initially takes a negative value directing the stationary fluid downward when the paddle is moving from its idle position toward the nozzle. At this stage, the y-force on the blocked region is still zero as visible in Fig. 24(b). However, as the paddle starts blocking the nozzle's outlet, positive y-force values emerge to counteract the strong negative vertical velocity generated by the counterclockwise rotating vortical

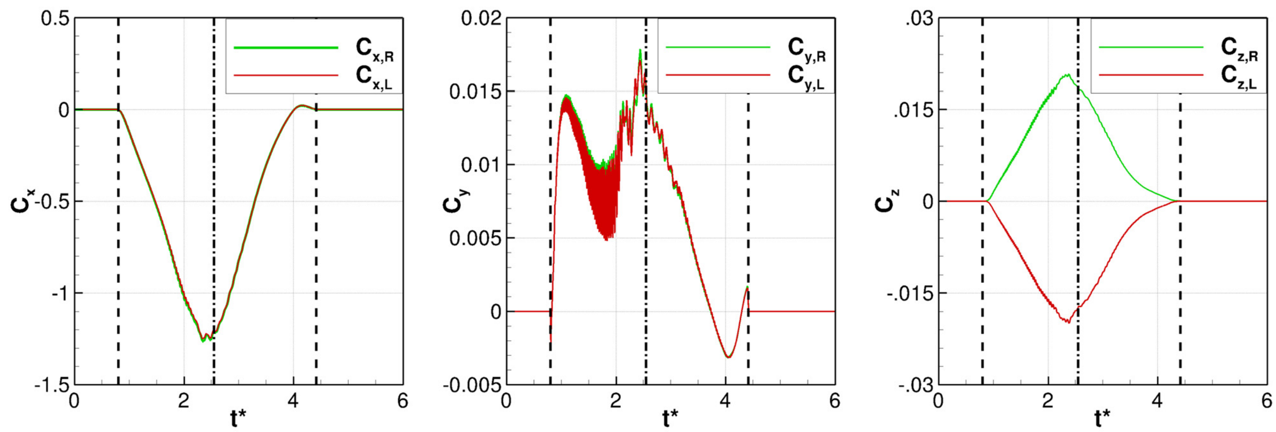

(a) x-force coefficient. (b) y-force coefficient. (c) z-force coefficient.

FIG. 24. Temporal evolution of the ensemble-averaged Lagrangian force coefficients focusing exclusively on the Lagrangian markers located in the region of the direct flow-paddle interaction [i.e., Fig. 22(b)]. Dashed lines mark Δt_{gust}, the dashed-dotted line marks the maximum blocking.

structure originating from the paddle's bottom edge [see the region behind the paddle at instant 2 in Fig. 10(b)]. Shortly thereafter, while the Lagrangian markers within the interaction region persist in directing the fluid upward [see Fig. 24(b)], an overall negative y-force component [see Fig. 23(b)] returns to oppose the high positive vertical velocity present in the gap between the paddle and the nozzle's outlet [e.g., see the fluid escaping in front of the paddle at instant 3 in Fig. 10(b)]. This means that two different effects work against each other in this phase of the paddle movement leading to this complex behavior of the y-component of the force. Even when the prescribed vertical velocity of the paddle becomes positive during the upstroke [see instant 5 in Fig. 10(b)], the paddle maintains its decelerating effect (obvious by an overall negative y-force component), indicating that the positive vertical velocity in the gap remains relatively high.

The z-component of the force coefficient on the entire paddle consistently maintains a value close to zero throughout the simulation time as depicted in Fig. 23(c). This behavior aligns with expectations due to the symmetric w-velocity pattern observed in Fig. 13(c). This is further supported by Fig. 24(c) where the right and left halves of Lagrangian markers within the interaction region exhibit a canceling effect.

VII. CONCLUSIONS

As demonstrated in the experimental study by Wood, Breuer, and Neumann,[1] a wind gust can be artificially generated in a wind tunnel by dipping a paddle into the free-stream leaving the nozzle. The paddle blocks the cross-section that leads to a rising velocity. The kinematics of the paddle determines the characteristics of the gust. In order to get a deeper insight into the paddle-flow interaction and the arising flow field, large-eddy simulations of the process are carried out. The motion of the paddle is described by the immersed boundary method relying on a direct forcing approach. Two sets of conclusions can be drawn from the study, one concerning the numerical method and the other related to the characteristics of the generated gusts.

A. Numerical method

- The original implementation of the immersed boundary method relying on an equidistant distribution of the Lagrangian markers was found to be very intensive concerning the required computational time since the spacing between the markers is dictated by the minimum local Eulerian grid. Furthermore, the markers are very unevenly distributed across the parallel processors, which also deteriorates the computational speed significantly.
- Introducing a non-uniform distribution of the markers in the spanwise direction with one marker assigned to each cell center strongly reduces the computational effort by about one order of magnitude, whereas the results obtained are nearly identical.
- Analyzing the results and especially the pressure distribution, it has to be mentioned that the IB method guarantees a smooth pressure field without any numerically induced oscillations when the paddle is moving in the fluid stream.
- The IB method employed assures the rigorous conservation of the force and moment coefficients. This underscores the fidelity of the numerical approach to the underlying physical principles delivering physically meaningful results.

B. Characteristics of the gust

- When the paddle enters the stream, the streamwise velocity rises and the flow is directed toward the ground plate. A strong vortex is generated at the bottom edge of the paddle and a new shear layer develops behind the paddle.
- At the maximum blocking ratio, the region above the ground plate reaches high streamwise velocities characterizing the resulting horizontal gust.
- When the paddle starts traveling back to its idle position, the large vortical structure reaches the ground plate and the gust strength already decreases again.
- An analysis of the spanwise distribution the generated gust shows symmetric velocity patterns for all velocity components. The homogeneity of the streamwise component of the predictions along the z axis is found to be in agreement with the experimental work of Wood, Breuer, and Neumann.[1]
- As speculated in Wood, Breuer, and Neumann[1] and now fully confirmed by the predictions, the undisturbed gust region limited by the neighboring shear layer is not very large, which has to be taken into account when using the gust generator for FSI studies in the wind tunnel.
- Due to the free shear layer and the high Reynolds number considered, the flow induced by the paddle's motion is dependent on the initial flow state at which the paddle starts to move. Thus, strong cycle-to-cycle variations are visible in both the experimental and numerical instantaneous data. In order to still be able to compare the results, an ensemble-averaging was conducted over several realizations.
- The agreement between measurements and predictions at specific locations in the flow field is found to be very good which confirms the quality of the simulations.

ACKNOWLEDGMENTS

The initial part of the project was financially supported by the *German Research Foundation* (*Deutsche Forschungsgemeinschaft*) under the Contract No. BR 1847/17-1, which ended already. Computational resources (HPC cluster HSUper) have been provided by the project hpc.bw, funded by dtec.bw—Digitalization and Technology Research Center of the Bundeswehr. dtec.bw is funded by the European Union–NextGenerationEU. Last but not least, we would like to thank Dr. J. N. Wood (HSU Hamburg) for providing the additional non-published measurement data[35] and fruitful discussions on the topic.

AUTHOR DECLARATIONS

Conflict of Interest

The authors have no conflicts to disclose.

Author Contributions

Khaled Boulbrachene: Conceptualization (equal); Investigation (lead); Methodology (equal); Software (lead); Validation (lead); Visualization (lead); Writing – original draft (equal); Writing – review & editing (equal). **Michael Breuer:** Conceptualization (equal); Funding acquisition (lead); Investigation (supporting); Methodology (equal); Project administration (lead); Resources (lead); Software (supporting);

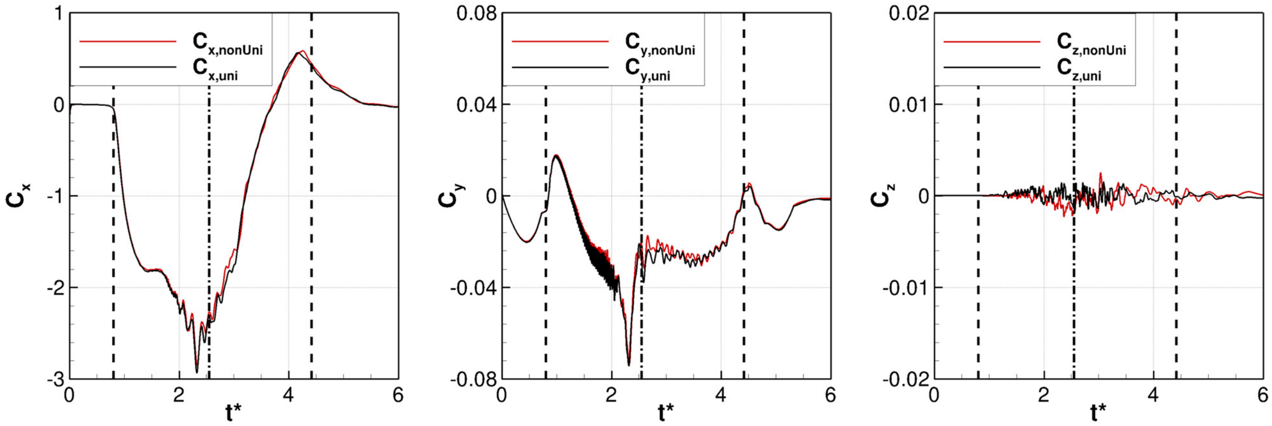

(a) x-force coefficient. (b) y-force coefficient. (c) z-force coefficient.

FIG. 25. Comparison of the instantaneous Lagrangian force coefficients between the simulation with the one-dimensional non-uniform distribution of Lagrangian markers (red) and its uniform counterpart (black). Dashed lines mark Δt_{gust}, the dashed-dotted line marks the maximum blocking.

Supervision (lead); Writing – original draft (equal); Writing – review & editing (equal).

DATA AVAILABILITY

The data that support the findings of this study are available within the article.

APPENDIX: COMPARISON OF FORCES FOR BOTH LAGRANGIAN MARKER DISTRIBUTIONS

In this section, the results obtained when the two different distributions of Lagrangian markers mentioned in Sec. V are used, is presented. Figure 25 depicts the instantaneous Lagrangian force coefficients of the simulation involving the one-dimensional non-uniform distribution of Lagrangian markers and its uniform counterpart. A detailed description of the computation of force coefficients is provided in Sec. VI D. The initial flow state, at which the paddle starts its motion, remains consistent for both simulations (here $t_{init} = 10\,s$). It can be observed that the deviations between the force coefficients between the different distributions are barely perceptible. This is particularly apparent in the x-force coefficient, which exhibits the highest order of magnitude. Despite discrepancies observed in the y- and z-force coefficients, these exhibit similar trends and are two orders of magnitude lower than the x-component, rendering them negligible. Since the forces applied by both distributions of Lagrangian markers on the flow exhibit a high degree of similarity, it is reasonable to anticipate a similar reaction from the flow for both distributions. Given the substantial difference in the computational time, the one-dimensional non-uniform distribution is preferred and consequently adopted throughout the results presented in this study.

REFERENCES

[1] J. N. Wood, M. Breuer, and T. Neumann, "A novel approach for artificially generating horizontal wind gusts based on a movable plate: The paddle," J. Wind Eng. Ind. Aerodyn. **230**, 105170 (2022).

[2] I. Neunaber and C. Braud, "First characterization of a new perturbation system for gust generation: The chopper," Wind Energy Sci. **5**, 759–773 (2020).

[3] H. H. Hu, N. Patankar, and M. Zhu, "Direct numerical simulations of fluid–solid systems using the arbitrary Lagrangian–Eulerian technique," J. Comput. Phys. **169**, 427–462 (2001).

[4] C. Peskin, "Flow patterns around heart valves: A digital computer method for solving the equations of motion," Ph.D. thesis (Albert Einstein College of Medicine of Yeshiva University, NY, USA, 1972).

[5] R. Mittal and G. Iaccarino, "Immersed boundary methods," Annu. Rev. Fluid Mech. **37**, 239–261 (2005).

[6] S. Majumdar, G. Iaccarino, P. Durbin *et al.*, "RANS solvers with adaptive structured boundary non-conforming grids," in *Proceedings of Annual Research Briefs* (Center for Turbulence Research, 2001), pp. 353–364.

[7] D. K. Clarke, M. D. Salas, and H. A. Hassan, "Euler calculations for multielement airfoils using Cartesian grids," AIAA J. **24**, 353–358 (1986).

[8] H. S. Udaykumar, R. Mittal, and W. Shyy, "Computation of solid-liquid phase fronts in the sharp interface limit on fixed grids," J. Comput. Phys. **153**, 535–574 (1999).

[9] H. S. Udaykumar, R. Mittal, P. Rampunggoon, and A. Khanna, "A sharp interface Cartesian grid method for simulating flows with complex moving boundaries," J. Comput. Phys. **174**, 345–380 (2001).

[10] C. S. Peskin, "The immersed boundary method," Acta Numer. **11**, 479–517 (2002).

[11] C. S. Peskin, "Numerical analysis of blood flow in the heart," J. Comput. Phys. **25**, 220–252 (1977).

[12] R. P. Beyer and R. J. LeVeque, "Analysis of a one-dimensional model for the immersed boundary method," SIAM J. Numer. Anal. **29**, 332–364 (1992).

[13] M.-C. Lai and C. S. Peskin, "An immersed boundary method with formal second-order accuracy and reduced numerical viscosity," J. Comput. Phys. **160**, 705–719 (2000).

[14] D. Goldstein, R. Handler, and L. Sirovich, "Modeling a no-slip flow boundary with an external force field," J. Comput. Phys. **105**, 354–366 (1993).

[15] E. Saiki and S. Biringen, "Numerical simulation of a cylinder in uniform flow: Application of a virtual boundary method," J. Comput. Phys. **123**, 450–465 (1996).

[16] C. Lee, "Stability characteristics of the virtual boundary method in three-dimensional applications," J. Comput. Phys. **184**, 559–591 (2003).

[17] P. Angot, C.-H. Bruneau, and P. Fabrie, "A penalization method to take into account obstacles in incompressible viscous flows," Numerische Math. **81**, 497–520 (1999).

[18]K. Khadra, P. Angot, S. Parneix, and J.-P. Caltagirone, "Fictitious domain approach for numerical modelling of Navier–Stokes equations," Int. J. Numer. Methods Fluids **34**, 651–684 (2000).
[19]E. Fadlun, R. Verzicco, and P. Orlandi, "Combined immersed-boundary finite-difference methods for three-dimensional complex flow simulations," J. Comput. Phys. **161**, 35–60 (2000).
[20]M. Uhlmann, "An immersed boundary method with direct forcing for the simulation of particulate flows," J. Comput. Phys. **209**, 448–476 (2005).
[21]A. Pinelli, I. Naqavi, U. Piomelli, and J. Favier, "Immersed-boundary methods for general finite-difference and finite-volume Navier-Stokes solvers," J. Comput. Phys. **229**, 9073–9091 (2010).
[22]J. N. Wood and M. Breuer, "The paddle: A novel procedure for artificial gust generation in a wind tunnel," in Proceedings of Gala–Fachtagung 'Experimentelle Strömungsmechanik', München, 5–7 September 2023, edited by C. J. Kähler, T. Fuchs, R. Hain, S. Scharnowski, B. Ruck, and A. Leder (2023).
[23]IEC-Standard, "Measurement and assessment of power quality of grid connected wind turbines," Technical Report No. IEC-61400–21, 2002.
[24]A. M. Roma, C. S. Peskin, and M. J. Berger, "An adaptive version of the immersed boundary method," J. Comput. Phys. **153**, 509–534 (1999).
[25]E. Anderson, Z. Bai, C. Bischof, S. Blackford, J. Demmel, J. Dongarra, J. Du Croz, A. Greenbaum, S. Hammarling, A. McKenney, and D. Sorensen, *LAPACK Users' Guide*, 3rd ed. (Society for Industrial and Applied Mathematics, Philadelphia, PA, 1999).
[26]F. Durst and M. Schäfer, "A parallel block-structured multigrid method for the prediction of incompressible flows," Int. J. Numer. Methods Fluids **22**, 549–565 (1996).
[27]P. K. Khosla and S. G. Rubin, "A diagonally dominant second-order accurate implicit scheme," Comput. Fluids **2**, 207–209 (1974).
[28]J. H. Ferziger and M. Perić, *Computational Methods for Fluid Dynamics*, 3rd ed. (Springer Berlin, 2002).
[29]C. M. Rhie and W. L. Chow, "Numerical study of the turbulent flow past an airfoil with trailing-edge separation," AIAA J. **21**, 1525–1532 (1983).
[30]M. Breuer, G. De Nayer, M. Münsch, T. Gallinger, and R. Wüchner, "Fluid-structure interaction using a partitioned semi-implicit predictor-corrector coupling scheme for the application of large-eddy simulation," J. Fluids Struct. **29**, 107–130 (2012).
[31]H. L. Stone, "Iterative solution of implicit approximations of multidimensional partial differential equations," SIAM J. Numer. Anal. **5**, 530–558 (1968).
[32]J. Smagorinsky, "General circulation experiments with the primitive equations I: The basic experiment," Mon. Weather Rev. **91**, 99–165 (1963).
[33]F. Schäfer and M. Breuer, "Comparison of c-space and p-space particle tracing schemes on high-performance computers: Accuracy and performance," Int. J. Numer. Methods Fluids **39**, 277–299 (2002).
[34]L. F. Moody, "An approximate formula for pipe friction factors," Trans. ASME **69**, 1005–1011 (1947).
[35]J. N. Wood, "CTA measurements of the paddle case," private communication (2023).